ΠΑΝΕΠΙΣΤΗΜΙΟ ΚΡΗΤΗΣ

ΣΧΟΛΗ ΘΕΤΙΚΩΝ ΕΠΙΣΤΗΜΩΝ

ΤΜΗΜΑ ΕΠΙΣΤΗΜΗΣ ΚΑΙ ΤΕΧΝΟΛΟΓΙΑΣ ΥΛΙΚΩΝ

ΠΤΥΧΙΑΚΗ ΕΡΓΑΣΙΑ

Investigation of graphitic - Carbon Nitride (g-C$_3$N$_4$) dispersibility in Common Solvents

ΚΟΣΜΑΣ ΓΙΑΝΝΑΡΗΣ (1268)

ΕΠΙΒΛΕΠΩΝ: Αναπλ. Καθ. Κιοσέογλου Γεώργιος

ΗΡΑΚΛΕΙΟ ΚΡΗΤΗΣ

ΟΚΤΩΒΡΙΟΣ 2021

Abstract

The present thesis intends to investigate the dispersion behavior of graphitic – Carbon Nitride (g-C_3N_4) in different solvents. In this context, nineteen (19) different solvents were utilized covering a broad range of physical characteristics (e.g. polarity, boiling point etc.). Initially, the synthesized g-C_3N_4 was extensively characterized in powder form by Attenuated Total Reflectance (ATR-IR), Ultraviolet-visible (UV-vis) and Raman spectroscopy, as well as X-ray diffraction (XRD). Following the characterization of the material, dispersions were prepared through a tip-assisted ultrasonication process, followed by centrifugation. In this way, stable dispersions were prepared since the supernatants were easily separated from the sediment. In addition, the final concentration of the dispersed and exfoliated g-C_3N_4 flakes in each solvent was determined by the Beer-Lambert law. It should be highlighted, that this is the time that stable g-C_3N_4 dispersions were prepared in various solvents by tip-ultrasonication instead of the conventional bath-assisted one. Finally, the Hansen Solubility Parameters (HSP) of the material were calculated.

Περίληψη

Η παρούσα εργασία σκοπεύει στη διερεύνηση της συμπεριφοράς σχηματισμού σταθερών αιωρημάτων γραφιτικού νιτριδίου του άνθρακα (g-Carbon nitride) σε διάφορους κοινούς διαλύτες. Στο πλαίσιο αυτό, χρησιμοποιήθηκαν 19 διαλύτες, οι οποίοι καλύπτουν ένα ευρύ φάσμα διαφορετικών φυσικών χαρακτηριστικών όπως η πολικότητα, το σημείο βρασμού κτλ. Αρχικά, έγινε φασματοσκοπικός χαρακτηρισμός του υλικού σε μορφή σκόνης με τη χρήση φασματοσκοπικών τεχνικών (ATR-IR, UV-Vis και Raman) καθώς και μορφολογικός χαρακτηρισμός με περίθλαση ακτίνων Χ (XRD). Κατόπιν, έγινε παρασκευή σταθερών διασπορών με τη χρήση ακίδας υπερήχων και ακολούθησε φυγοκέντρηση όλων των διασπορών για τον τελικό διαχωρισμό του υπερκείμενου από το ίζημα. Στη συνέχεια, η τελική συγκέντρωση κάθε διασποράς προσδιορίστηκε μέσω του νόμου των Beer-Lambert σε κάθε διαλύτη ξεχωριστά. Αξίζει να σημειωθεί, ότι η παρούσα μελέτη είναι η πρώτη στη βιβλιογραφία στην οποία παρασκευάστηκαν σταθερές διασπορές του γραφιτικού νιτριδίου του άνθρακα σε μια τόσο ευρεία γκάμα διαλυτών με τη χρήση ακίδας υπερήχων αντί του συμβατικού λουτρού υπερήχων. Τέλος, υπολογίστηκαν οι παράμετροι διαλυτότητας Hansen (HSPs) του υλικού.

To Sofia

Break off my arms, I'll take hold of you
with my heart as with a hand.
Stop my heart, and my brain will start to beat.
And if you consume my brain with fire,
I'll feel you burn in every drop of my blood.

R. M. Rilke

Table of Contents

Chapter 1: Carbon Allotropes

1.1 Doped carbon-based structures

Doping with various heteroatoms, such as nitrogen (N), phosphorus (P), boron (B) and sulfur (S), is one of the most well-known strategies towards the adjustment of the electronic and chemical properties of carbon-based materials, like graphite, graphene, porous carbon, carbon nanotubes etc. Among them, N-doped graphene is the most studied and used in various applications (photodegradation, CO_2 reduction, photocatalysis etc.).[1]

In general, as in the case of graphene, carbon substitution by nitrogen may result in the formation of three possible N-doped heterostructures, named as pyridinic, pyrrolic and graphitic, as depicted in **Figure 1a**. Pyridinic-N atoms are bonded with two C atoms and constitute a part of a hexagon, while the Pyrrolic-N ones are bonded with two C atoms forming a pentagon. Both types may exist at the edges of the flake, but also it is possible to be located on the basal plane when defects (holes) exist on the lattice (see **Figure 1a**).
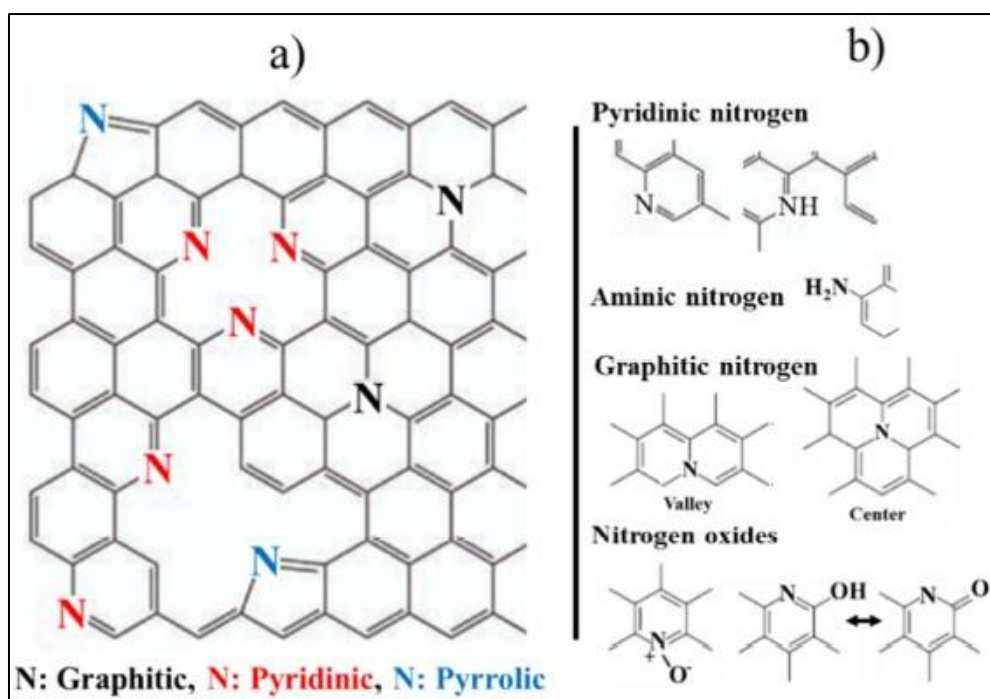
Figure 1: Representation of different modulations of N-doping for a) graphene and b) their individual structure.[1]

On the other hand, the graphitic type of N atoms exists when an sp^3 hybridized carbon atom is replaced by nitrogen and thus it can be located on the basal plane of the flake (also see **Figure 1a**). More specifically, there are two forms of graphitic-N atoms; close to the edges which is called "valley" and at more interior regions of the flake, called as "center". In addition, two types of pyridinic-N may exist, depending on the presence or absence of hydrogen, respectively. It should be noted that some nitrogen oxides or aminic nitrogens can be located at the edges of the flake (**Figure 1b**).[1]

Sulfur as dopant

Sulfur (S) doped carbon-based materials have also attracted great interest in many research fields. According to a similar reaction mechanism as in the case of nitrogen, sulfur atoms may substitute carbon atoms on the graphene honeycomb, as part of the pentagonal or hexagonal rings. Therefore, S atoms can be located either on the basal plane or at the edge of the graphene lattice.[2,3]

S-doped graphene can be synthesized according to a solvothermal method using S-rich organic precursors, such as benzyl disulfide (BDS), DMSO, etc. (**Figure 2**).[3] S-doped graphene can be also produced through electrochemical synthesis, since C atoms can be replaced by S atoms via electrochemical doping, as presented in **Figure 3**.[2]
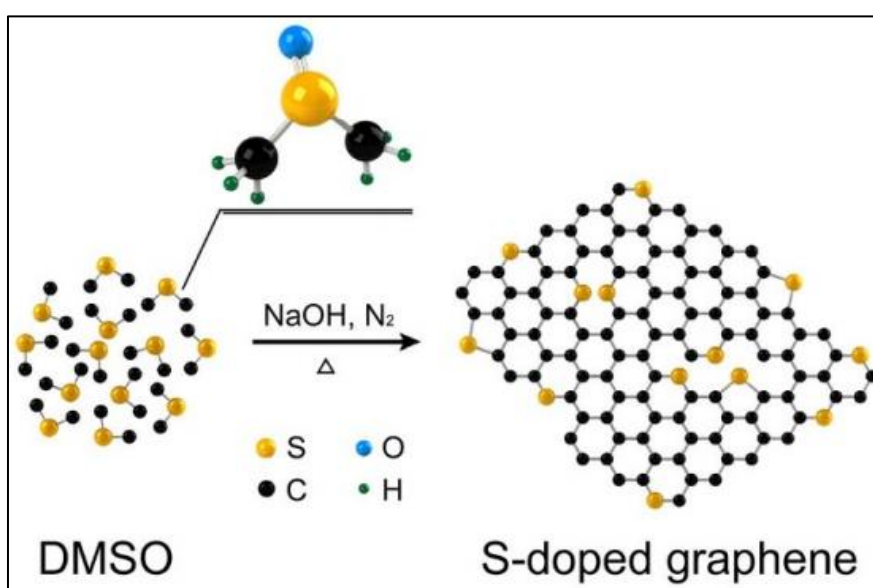
Figure 2: Illustration of the solvothermal synthesis of S doped graphene.[3]
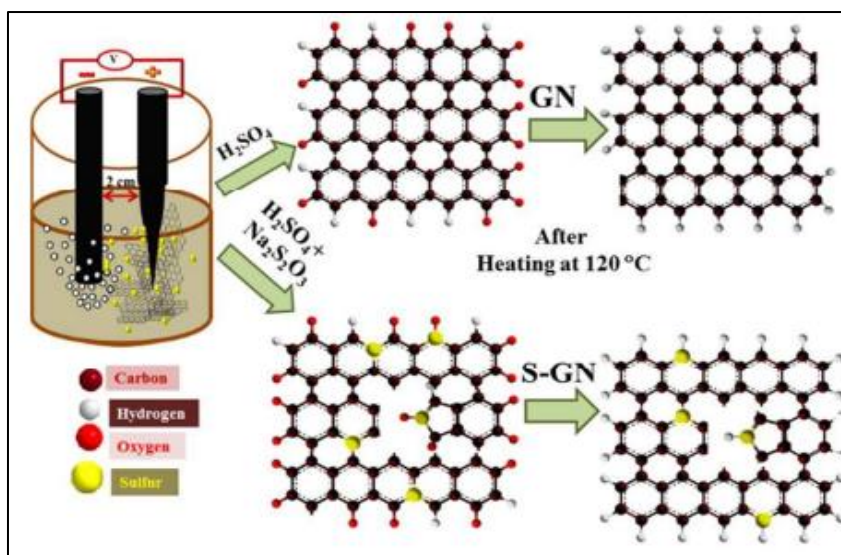
Figure 3: The electrochemical synthesis of S-doped graphene.[2]

Boron as dopant

Except from nitrogen and sulfur, boron (B) is a very commonly used doping element as well, due to its high applicability in many electronic devices.[4] B-doped graphene can be obtained through an arc discharge of graphite-based electrodes in the presence of diborane as the source of B atoms. As a result, B atoms easily substitute the carbon ones on the graphene lattice and thus B-doped graphene is produced (**Figure 4**).[4]

Figure 4: Boron doped graphene synthesis through arc discharge method.[5]

However, the most common approach to prepare B-doped graphene is a solid-state reaction between the graphene oxide (GO) and boric acid (H_3BO_3). GO and H_3BO_3 can be treated and annealed at high temperatures (900 - 1200 ^oC) under inert conditions (Ar_2 atmosphere). After the treatment of GO with H_3BO_3 and the formation of the composite, B-doped graphene is produced upon reduction, according to conventional reduction methods used to yield graphene from graphite oxide (**Figure 5**).[4,6]
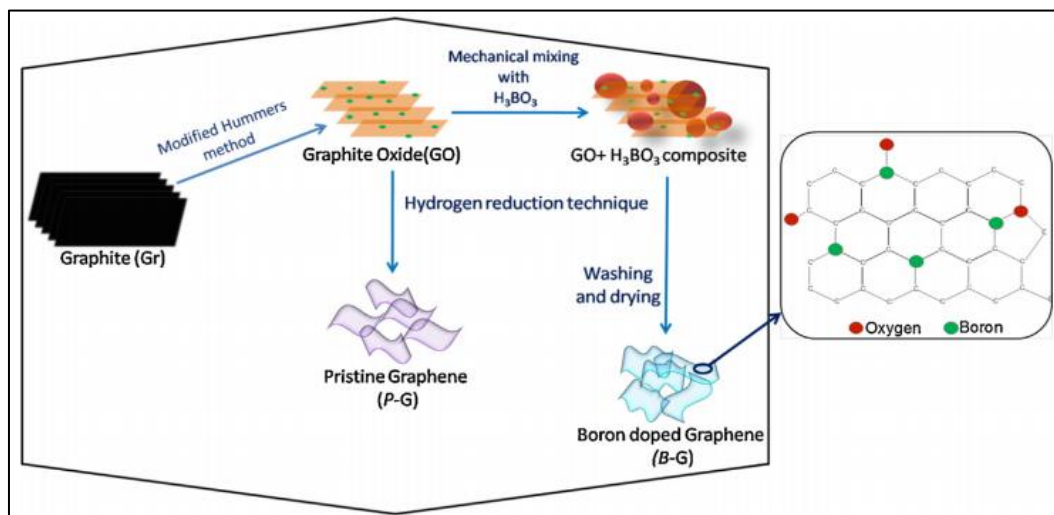
Figure 5: The synthesis of boron doped graphene through a solid-state reaction.[7]

Phosphorus as dopant

Phosphorus (P) doped carbon-based materials are mostly used in catalytic applications due to their superior catalytic properties. Their preparation is simple and facile; therefore, the introduction of P molecules into carbon-based materials nanosheets (i.e. graphene) is considered as an effective way to alter its chemical properties, resulting in materials with desired abilities and specified applications.[7] Their preparation process is similar to the doping of graphene-based materials with B, where GO prepared by a modified Hummers' method is treated with a mixture of phosphoric acid/triphenyl phosphine, under the same reaction conditions.[8,9] More precisely, the doping of graphene with P heteroatoms can change its electronic and magnetic properties, as well as its chemical reactivity, thus expanding its applicability to a variety of applications such as energy storage applications, electrocatalysis of oxidation reduction reaction (ORR) and hydrogen generation (**Figure 6**).[8,9]
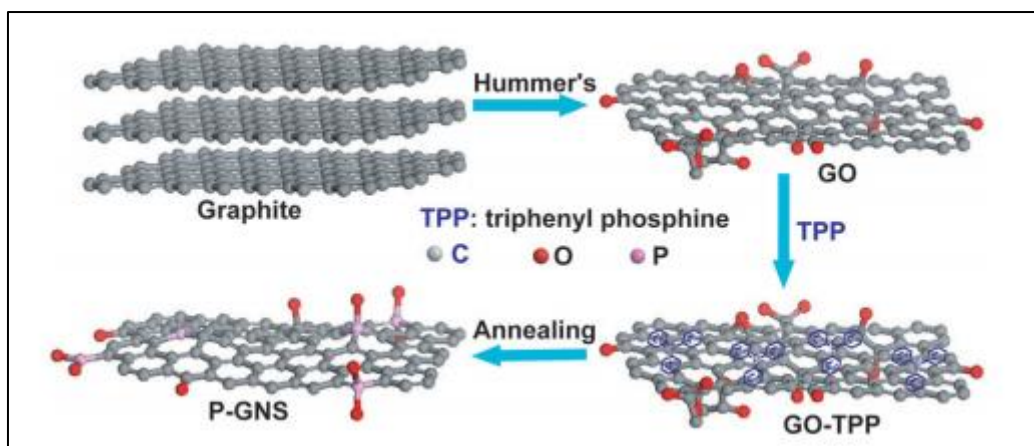
Figure 6: The schematic illustration of P doped graphene synthesis.[9]

1.2 Properties of (Doped) Carbon Allotropes (optical/electrical/catalytic)

Catalytic properties

Carbon-based materials when doped with various heteroatoms exhibit outstanding catalytic activity and are widely used as electrocatalysts in ORR, as mentioned above. Although the most commonly doped carbon-based materials are the N-doped ones, there are only few articles in the literature reporting on their high electrocatalytic performance for ORR. On top of that, the majority of the articles note that the presence of alkaline electrolytes is highly required.[10] In this direction, studies by Dai et al.[11] and Que et al.[12] presented higher catalytic performance using doped carbon materials for ORR in alkaline solute, compared to platinum-based catalysts, although their potential onset remained lower contrary to the current density which was three times higher.[12]

Even though the catalytic properties of P-doped carbon-based materials have been extensively studied, it is shown that their catalytic efficiency is not as profitable as in the case of doping with N. Studies by Liu et al.[13] and Guo et al.[14] demonstrated that P-doped graphene showed an improved potential onset and larger current density compared to pristine graphene. P atoms may result in a efficient modification of the chemical reactivity of carbon-based materials due to their ability to form stable catalysts in basic and acidic media something that can be useful in many applications, like for example in catalysis.[15,16]

As in the case of P atoms, B atoms are less electronegative than the nitrogen and carbon ones when exist within B doped carbon-based materials, and thus they are basically considered as ideal components for CO_2 splitting reactions. Some studies suggested that the catalytic activity of B atoms in ORR is very similar

6

with the one achieved when conventional catalysts based on Pt nanoparticles are utilized. It is speculated that the overall catalytic efficiency is assigned to the electron deficiency of B atoms.[17,18,19,20]

Despite the limited number of studies, it is apparent that S-doped graphene-based materials are ideal for ORR catalysis.[10] In this context, Yang et al.[21] proposed that S doping may increase defects at the edges and structural disorder of the graphene basal plane. Therefore, improvements in ORR and changes in spin density can be observed. Other articles suggest that the defects formed onto the graphene honeycomb, due to the presence of S atoms, may result in enhanced ORR activity.[22]

Moreover, doped carbon materials can be exploited for H_2 generation produced by catalytic reactions, fuel cells and other water splitting applications. It is considered as the safest, greenest and lowest-cost method for H_2 production especially when the necessary energy is produced by renewable sources such as wind and solar power. Finally, the method is very appealing as water is abundant and the only byproduct is O_2, a non-harmful and rather useful substance.[23]

Electrical properties

Many studies have focused on the improvement of the electrical properties of graphene.**Error! Bookmark not defined.** Shih et al. reported on the capability of the doping elements used to successfully modify these properties. This can be confirmed by calculating the band structures of doped graphene with different dopants (Si, B, N).**Error! Bookmark not defined.** The substituted atoms could drastically change the electrical properties by broadening the zero energy band gap of graphene. It is reported that the band gap is opened at the Dirac point and its size depends on the concentration, the atomic configuration and especially the type of the dopant, since there is a Fermi level shifting depending on the dopants' electronegativity. **Error! Bookmark not defined.**,[25]

Optical properties

Shih et al. also investigated the optical properties of doped graphene and proposed that high doping concentrations can modify the number of energy sub bands and shift the Fermi level.**Error! Bookmark not defined.** More energy bands near zero-energy can be observed with the increase of dopants concentration. As for the Fermi level, it is unaffected when a material is doped with Si but downshifts when doped with B or S and upshifts in case of doping with N, respectively.**Error! Bookmark not**

Therefore, due to the above modifications, more excitation channels can be observed between the occupied valence and unoccupied conduction electronic states while many of them exhibit similar energy. Finally, with the increase of the dopants' (Si, N, B) concentration, a reduction in the overall spectral intensity can be observed. **Error! Bookmark not defined.**

Chapter 2: Carbon nitride

2.1 The structure of carbon nitride

Graphitic carbon nitride has attracted a lot of attention due to its unique optoelectronic properties and its high applicability in various fields (photovoltaics, biosensing, photocatalysis etc.).[24] It is a two dimensional material beyond graphene (**Figure 7**) that consists of a regular arrangement of triazine units.[24] In 1996 it was predicted that carbon nitride has five different structures including α-C_3N_4, β-C_3N_4, c-C_3N_4, p-C_3N_4 and g-C_3N_4 (**Figure 8**). Apart from g-C_3N_4, the other four structures belong in super hard materials and thus it would be easier for graphitic carbon nitride to be customized.[25] Two condensation states can be distinguished as the major structural units of a single sheet of the g-C_3N_4; the first one consists of s triazine units with a regular position of the single carbon vacancies while the second one is formed by tri s triazine/heptazine compounds. In the literature it is mentioned that the tri-s-triazine-based g-C_3N_4 is more stable than the s-triazine-based one (**Figure 9**).[1]
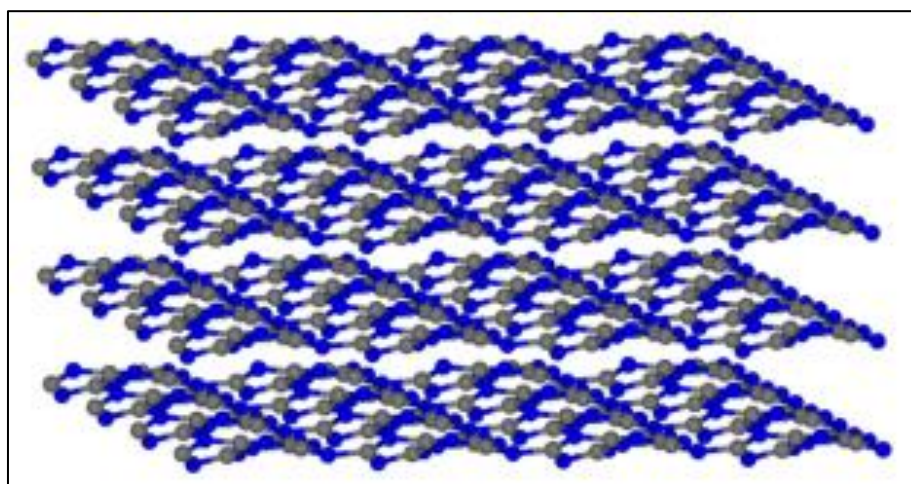
Figure 7: The structure of bulk g-C_3N_4[26] (the gray color represents C and the blue one N, respectively).
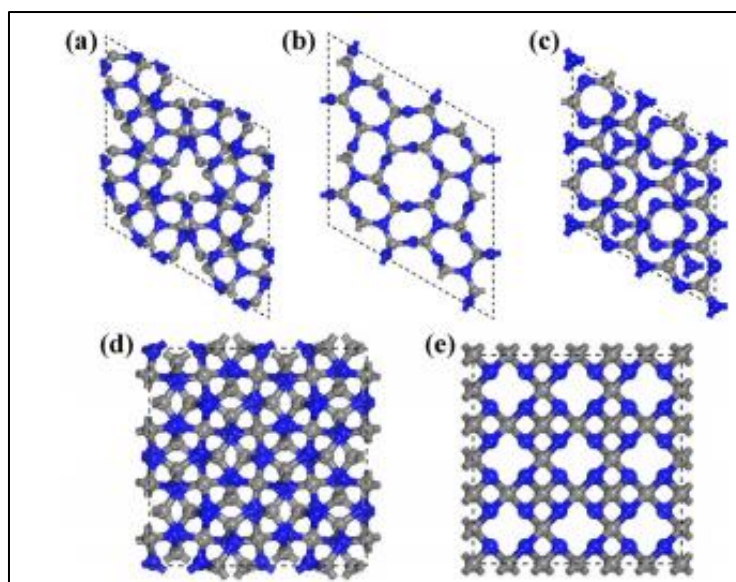
Figure 8: The structures of (a) α-C_3N_4, (b) β-C_3N_4, (c) g-C_3N_4, (d) cubic-C_3N_4 and (e) pseudocubic-C_3N_4.[25]
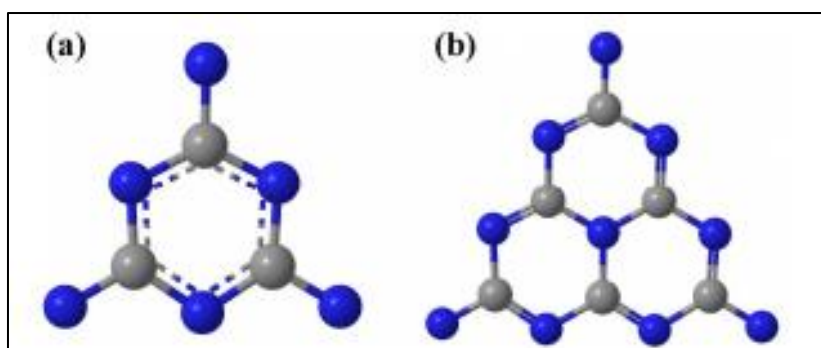
Figure 9: a) Triazine and b) tri-s-triazine based connection patterns.[25]

2.2 Preparation of carbon nitride

The most common and efficient methods for the preparation of g-C_3N_4 are top-down and bottom-up methods. The bottom-up approach refers to the creation of nanoparticles through chemical reactions between atoms, ions and molecules. On the contrary, methods for crushing or breaking the bulk material into many components to create nanoparticles are used in the top-down approach (**Figure 10**).[27]
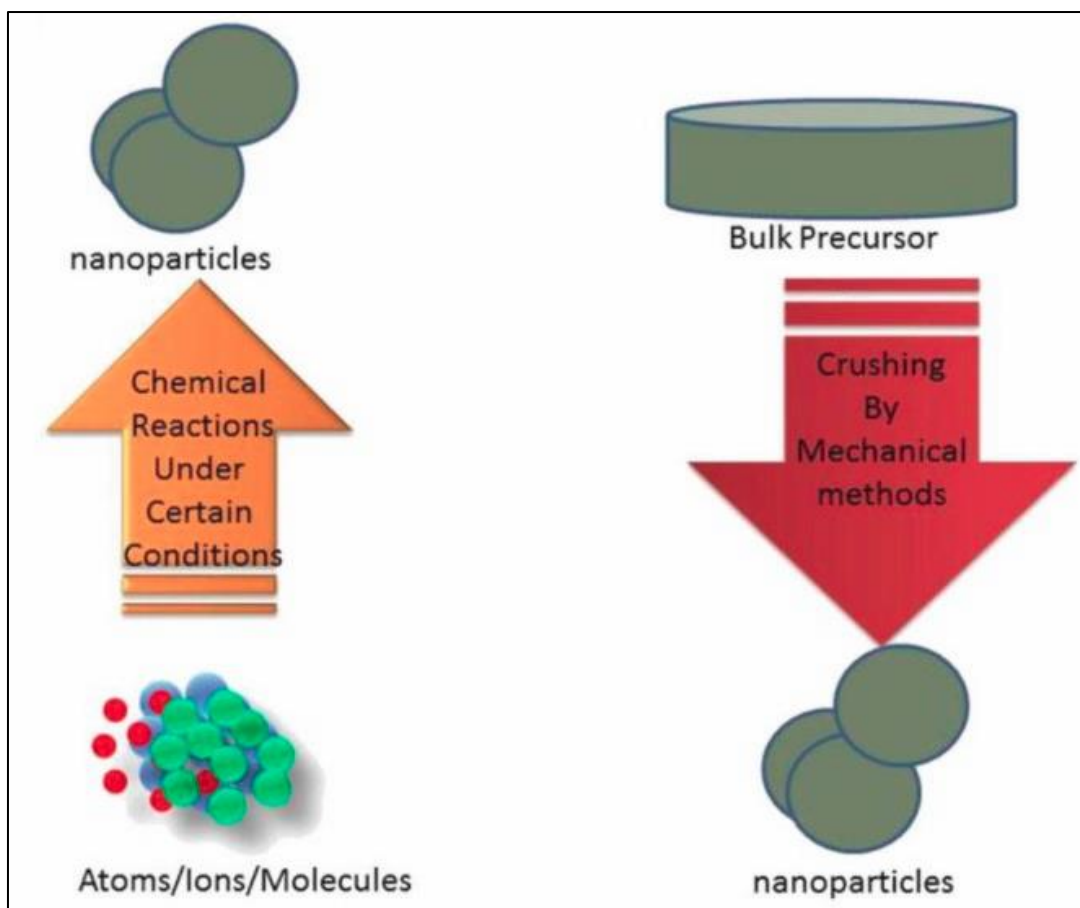
Figure 10: Bottom-up and top-down preparation methods [27]

2.2.1 Top-down methods:

The calcination method

This method intents to weaken the Van der Waals forces between the layers of bulk $g\text{-}C_3N_4$.[25] Calcination occurs upon the heating of solids, towards the removal of volatile compounds, even the oxidation of mass etc.[28] Studies by Niu et al. and Li et al. proposed an optimum calcination temperature for $g\text{-}C_3N_4$ nanosheets up to 500 $^{\circ}$C.[29,30] By heating the bulk material under Ar_2 or ammonia gas, nanosheets with improved catalytic properties can be produced (**Figure 11**).[25]
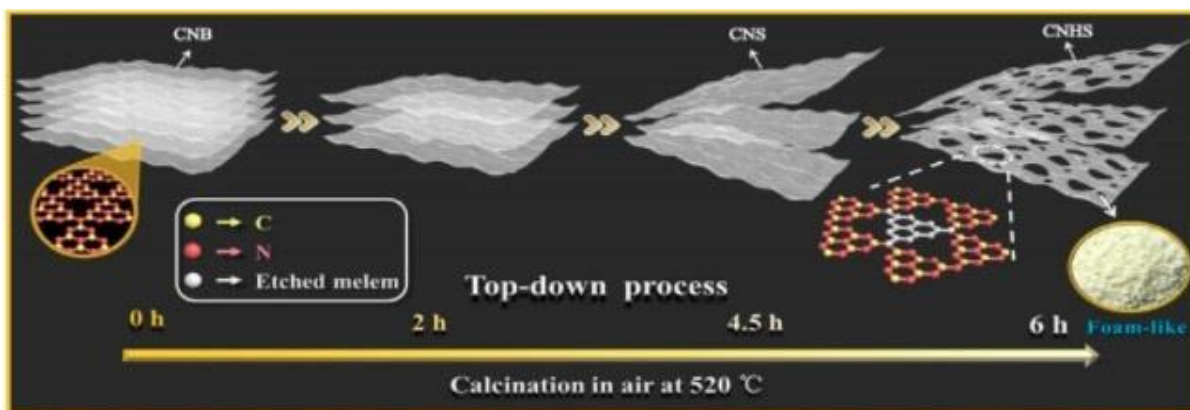
Figure 11: The calcination process followed for g-C_3N_4 nanosheets synthesis. [25]

Liquid phase exfoliation

Liquid phase exfoliation (LPE) is a simple approach assisted by the application of an external force (ultrasonic wave, pressure or thermal energy) and is considered as suitable for the preparation of low dimensional materials.[25] To evaluate the degree of exfoliation, two critical factors should be taken into account; a) the solvent and b) the energy input. Due to the presence of Van der Waals interactions between the layers of the bulk material, an energy barrier should be overcome in order the exfoliation to take place. Therefore, it is obvious that the exfoliation degree may vary, depending on the solvent medium characteristics (surface tension, boiling point, polarity etc.).[31] Among the common solvents used (water, DMF, ethanol, methanol, THF), water is the most appropriate solvent due to its higher polarity.[25]
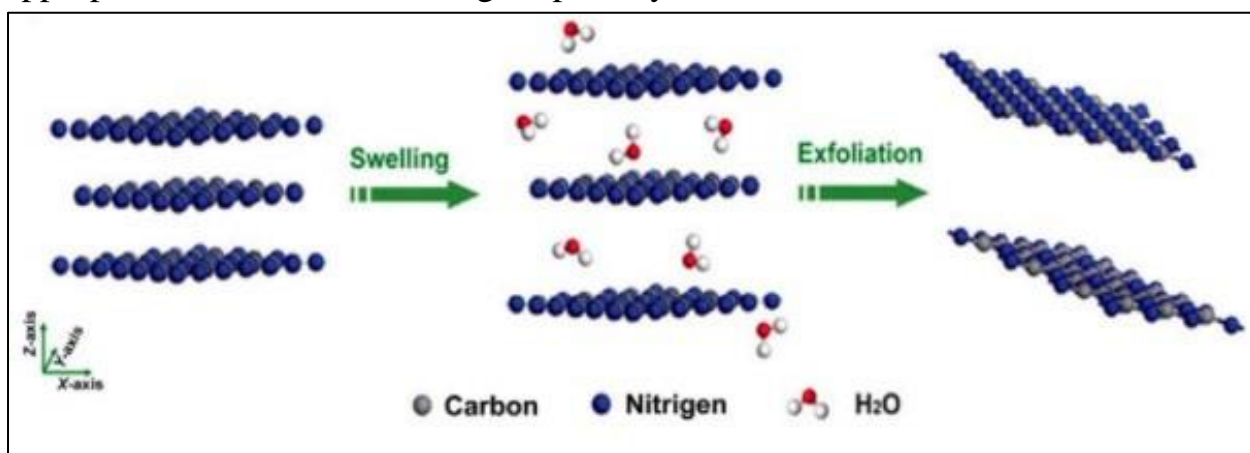
Figure 12: Liquid phase exfoliation of bulk g-C_3N_4.[25]

Except from the selected solvent's characteristics, the applied energy input on the bulk material, using bath or probe assisted sonication, may also affect the degree of exfoliation. This is due to the shear forces and cavitation bubbles, originated

by the ultrasounds, which can completely or partially exfoliate the multi-layered bulk materials to few or single layered ones (**Figure 12**).[25,31]

2.2.2 Bottom-up methods:

Condensation

g-C_3N_4 can be produced by simple condensation methods. Wang et al. proposed a three-step condensation reaction of dicyandiamide (DCDA) which includes the removal of ammonia upon thermal treatment, thus promoting the formation of g-C_3N_4 network. Throughout the condensation, the rejection of ammonia forces nitrogen compounds to self-assemble into melamine at 240 °C and consequently into melem at 390 °C, which respectively may result in the formation of g-C_3N_4 network at 520 °C (see **Figure 13**).[32]
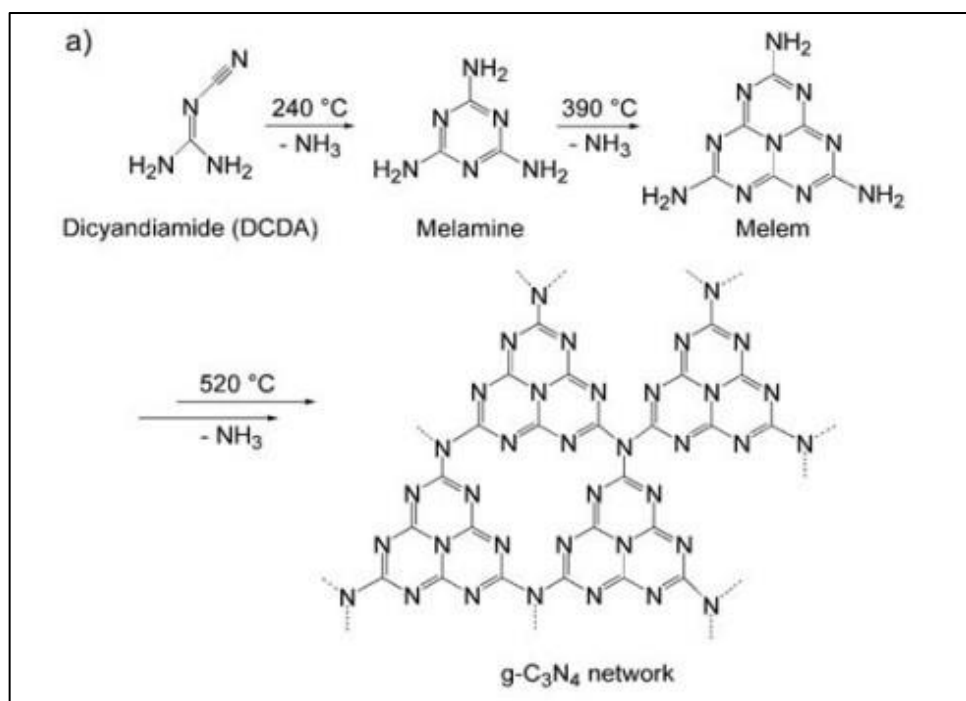
Figure 13: The condensation reaction from DCDA to g-C_3N_4.[32]

Another condensation strategy proposed by Motigaud et al. [33] and Park et al. [34] includes the preparation of graphitic carbon nitride upon the condensation of melamine with cyanuric chloride in the absence of HCl.

Solid state reaction

A solid-state reaction can be carried out through contact, nucleation, reaction and crystal growth between solid materials at high temperatures.[25] Kouvetakis et al. successfully used a solid-state reaction to produce C_3N_4 thin films using 2,4-difluoro-6-bis(trimethylsilyl)imido-l,3,5-triazine and 2,4-dichloro-6-bis(trimethylsilyl)imido-1,3,5-triazine as precursors.[25]

Morphology, crystallinity, dimensionality and properties of g-C_3N_4 may differ due to variations in the synthetic parameters such as the temperature and pressure.[25] According to the literature, in many reactions the change of one parameter may alter the material's properties as stated by Zhang et al.,[35] Gu et al.,[36] Lu et al.[37] etc. It should be noted that the solid-state reaction it is not widely used, since high temperature and pressure are required. Thus, it is considered as an expensive and not ecofriendly approach.

Electrochemical deposition

Electrochemical deposition is the process of depositing one substance onto the surface of another using oxidation and reduction, and electrodes are used to introduce electricity to an electrolyte solute during the process. After a certain time, the ions of the deposition material, adhere onto electrodes. This process can form very thin coatings and thus it is considered as cost-effective (**Figure 14**).[38] This technique is well known and used due to its capability to improve the properties and the quality of products. In this frame, the properties of g-C_3N_4 can be modified using numerous precursors in different solvents.[25]
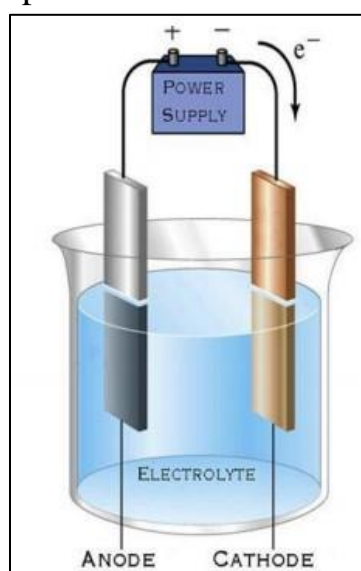
Figure 14: The electrochemical deposition.[39]

The solvothermal reaction

Solvothermal is a method in which a reaction between the original mixture and an organic or non-aqueous solvent takes place into a sealed system at certain pressure and temperature conditions. As a result, the products of the reaction exhibit high crystallinity, uniform morphology and good dispersibility.[25] The first synthesis of g-C_3N_4 according to this procedure was made by Montigaud et al. who used melamine and cyanuric chloride in triethylamine under 130 MPa and 250 °C. Any differentiation in the solvent and the reaction conditions may yield in g-C_3N_4 with different crystallinity, morphology and dispersibility.[25]

Thermal decomposition

Thermal decomposition of cyanuric triazide (2,4,6-triazido-1,3,5-triazine) is an endothermic reaction in which chemical decomposition occurs by heating in high temperature and pressure.[40] It is the most common method used to produce large quantities of g-C_3N_4 due to its ease of processing, the abundance of resources and its low cost. In order to modify tricyanomelaminate and to obtain g-C_3N_4, Lotsch and Schnick used ammonium, guanidinium and melaminium, as depicted in **Figure 15**.[25]
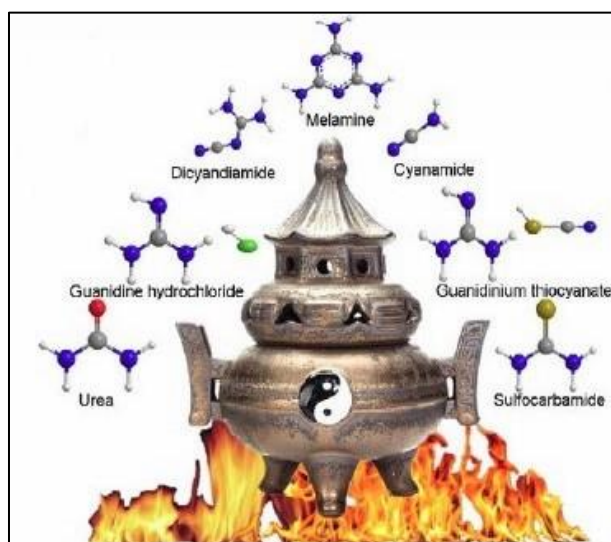
Figure 15: Schematic representation of thermal decomposition.[25]

2.3 Properties of carbon nitride

Electrical properties

Graphitic carbon nitride has attracted a lot of attention among the 2D nanomaterials due to its unique physicochemical properties.[41] Mortazavi et al. experimentally determined its band gap at 2.7 eV, indicating its highly promising applicability in optoelectronic devices.[41]

In a related context, Konofaos et al. [42] and Derradji et al.[43] explored that carbon nitride thin films with higher nitrogen content exhibited lower resistivity and higher dielectric constant respectively compared to the lower nitrogen content ones. Derradji et al. also demonstrated a proportional relationship between conductivity and the content of the nitrogen atoms existed in a g-C_3N_4 film, since higher percentage of nitrogen atoms implies higher conductivity. However, it should be noted that this relationship exists only in the case that the nitrogen concentration (nitrogen atoms) is up to 18%.[43]

Optical properties

As for the optical properties, Giusto et al. observed that carbon nitride films exhibited the highest intrinsic refractive index (n_D=2.43) for polymers to date. [44] g-C_3N_4 films highly emit blue fluorescence under UV irradiation. The photoluminensce (PL) spectra of the films differs from that in powder form due to the manifold transitions between different energy levels in light stimulation. Similarity in the spectra of the two forms can be observed when the film thickness is over 1 μm due to the increased condensation of the forerunner.[44]

Anisotropy

Carbon nitride films that are synthesized through condensation, possess anisotropic properties due to the substrate effect during the deposition process.[45] Arazoe et al. noted that there is a larger gradient at the edges of the film, due to the unreacted amino groups compared to the basal plane.[46] Moreover, Jia et al. pointed out that the side of the substrate seems to be thicker than the growing side due to the great impact of the flat substrate during the deposition process.[47]

Mechanical properties

Mechanical properties, in terms of flexibility, were studied by Cai et al. who used a strip consisted of a g-C_3N_4 based coating (10 μm thickness, 3 cm width, 1.5 cm length) in test conditions of clamping and stretching at a certain speed. The film strip exhibited a tensile strength up to 0.1 GPa and could elevate a 25,000 times heavier object.[48] Arazoe et al. reported, following nanoindentation analysis, that the reduced Young modulus and the hardness of the strip are 12GPa and 1GPa, respectively.[46] Carbon nitride strip was also pliable and could remain intact after continuous bending and unbending distortions.[48]

Catalytic properties

As mentioned above, g-C_3N_4 has been widely used in photocatalytic applications due to its ability to harvest solar energy.[49] Thanks to its "green" properties like non-toxicity and high recyclability, g-C_3N_4 could ideally replace the conventional TiO_2 based photocatalysts, which are harmful to humans and animals when being inhaled. However, low absorption in visible light, fast recombination of the excited electrons and low surface area remain a bottleneck towards its extended use.[49]

In the field of electrocatalysis, carbon nitride can be applied in Hydrogen Evolution Reaction (HER) due to its superior electrochemical properties. HER technology is based on water splitting via electrolysis producing molecular hydrogen; therefore, electrocatalyst materials are required.[50] Due to restricted resources and the high cost of Pt-based catalysts, the most widely used in electrocatalytic reactions metal free catalysts have attracted a lot of interest thanks to their high reactivity and their great availability. In this context, g-C_3N_4 can be considered as an excellent stable and efficient electrocatalyst mainly thanks to its electronic structure, its high nitrogen content and its unique thermal and chemical properties.[51]

2.4 Absorption coefficient of carbon nitride

The optical absorption and the bandgap of g-C_3N_4 depends on several factors such as the thickness, the size of flakes, as well as the concentration in case of dispersion etc.[52] As Varela et al.[53] examined, the UV-vis spectrum of g-C_3N_4 dispersion displays a broad peak at ~230 nm, a characteristic strong peak at 320 nm and a weak shoulder at ~390 nm (see **Figure 16**), which is in full agreement with previous articles in the literature.[54] The shoulder can be assigned to the π→π* transitions of C=N structures in the tris-s-triazine unit. The peak at 320 nm

is attributed to the n→π* transitions from the nitrogen lone pairs of the amine groups located at the edges or to the extended tri-s triazine structure.[53] In general, the absorption coefficient value for g-C_3N_4 varies depending on the number of layers per flake, the lateral size and the amount of the amino groups presented on the lattice.[53] It should be noted that there is no representative absorption coefficient value for g-C_3N_4 reported in the literature.
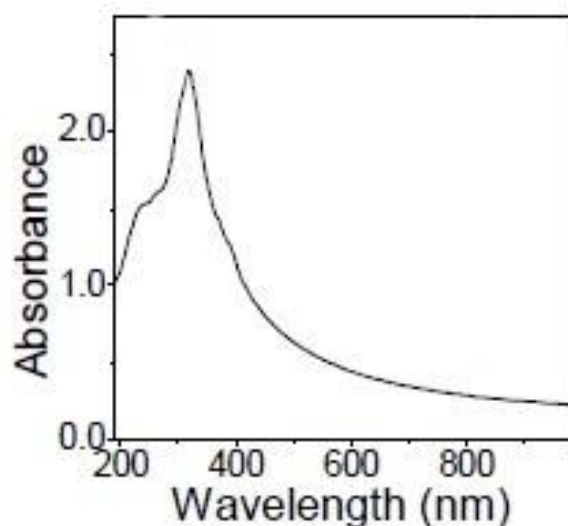
Figure 16: A characteristic absorption spectrum of g-C_3N_4 in DMSO.[53]

2.5 Applications of carbon nitride

Catalytic applications

The photocatalysts based on g-C_3N_4 are mainly used a) for pollutants' degradation and for water splitting applications.[25] According to Qian et al., g-C_3N_4 nanosheets presented a higher surface area and better optical properties compared to the bulk material, exhibiting a band gap of 2.7 eV.[25] In another study by Niu et al., g-C_3N_4 nanosheets were used as the catalyst material to split water and generate hydrogen.[55]

Moreover, the photocatalytic reduction of nanosheets can promote the conversion of CO_2 to chemicals and fuels (e.g. methanol fuel, methane, acetic acid).[56] As shown, the adsorption energy of CO_2 molecules was reduced from -0.99 to -1.37 eV upon the use of g-C_3N_4 nanosheets instead of the bulk form. Moreover, since g-C_3N_4 nanosheets tend to exhibit larger specific area than the bulk material, more active sites exist and thus enhanced photocatalytic activity (see in **Figure 17**).[25]
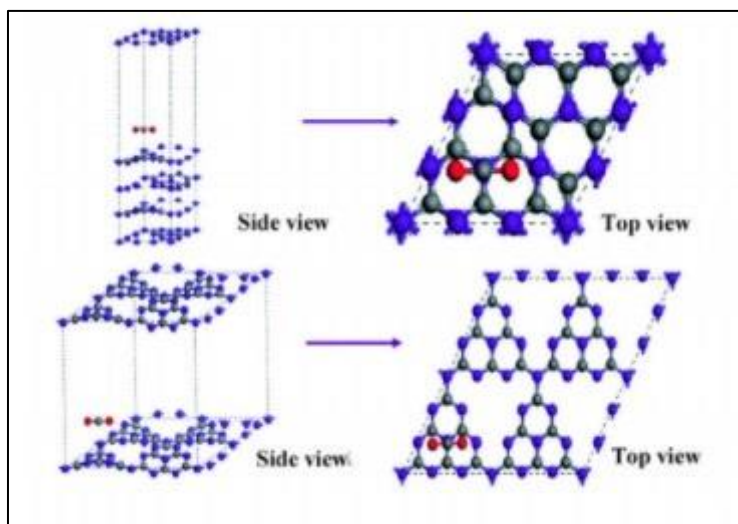
Figure 17: Schematic representation of CO_2 adsorption on a g-C_3N_4 nanosheet (top) and bulk g-C_3N_4 (bottom).[25]

Environmental applications

g-C_3N_4 nanosheets have been extensively incorporated in various environmental applications due to their superior capability to photodegrade many organic pollutants such as phenol, rhodamine B (RhB), tetracycline or 2,4-dichlorophenol.[25] The photocatalytic oxidation of the nanosheets can be also used for sterilization and self-cleaning applications.[25]

Sensor applications

g-C_3N_4 nanosheets display high fluorescence quantum yield and high specific surface area and therefore, they can be incorporated in sensing applications.[57] In this framework, Zhang et al. designed and developed a g-C_3N_4 nanosheet–MnO_2 composite based sensor. The developed sensor was very fast and accurate for the detection of glutathione in aqueous solutions, as displayed in **Figure 18**.[57]
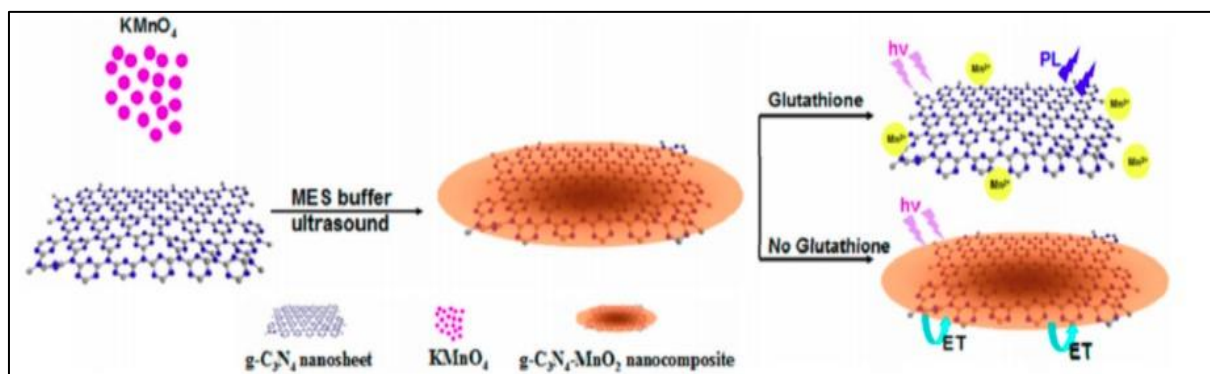
Figure 18: g-C_3N_4 nanosheet–MnO_2 composite for sensing glutathione [57]

Energy applications

g-C_3N_4 can be used in energy storage applications, as well. Wu et al. proposed that high density lithium can be interposed into the triangular space between the triazine units of g-C_3N_4. In this context, it was reported that interconnection between Li atoms and nitrogen spaces is very strong and thus it could be ideal for energy storage.[57] In addition, lithium-carbon nitride composites can be used either as the anode or the cathode material in lithium-based batteries providing great potential for hydrogen storage, since the hydrogen adsorption energy of lithium is ideal for hydrogen sorption (**Figure 19**).[57]
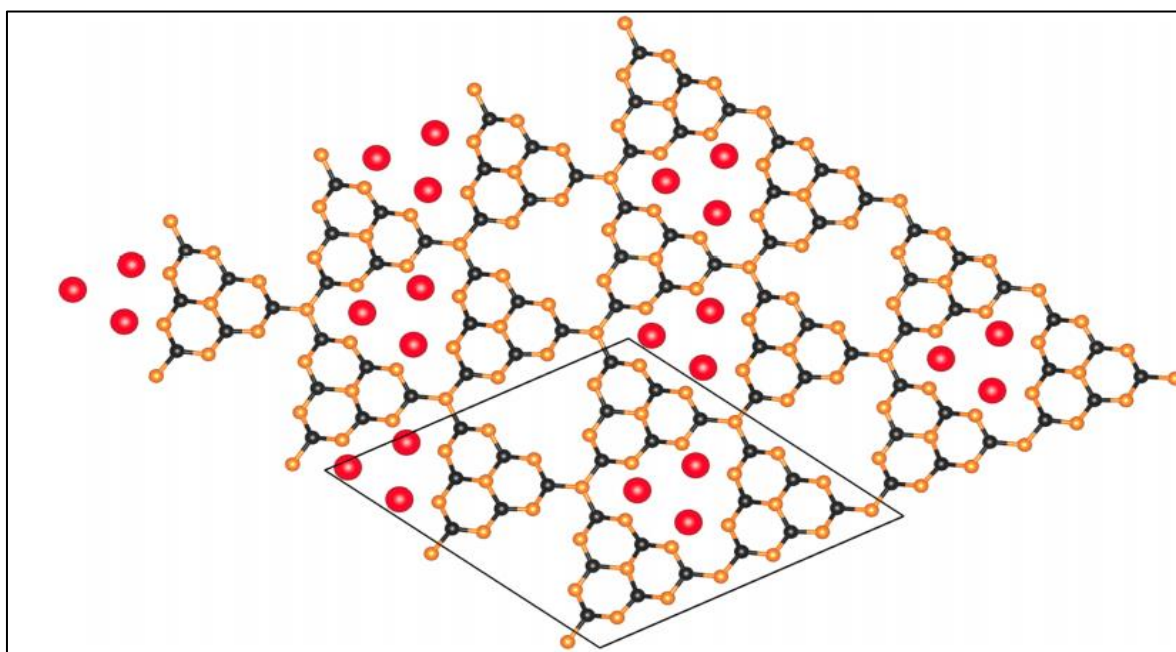
Figure 19: Lithium- g-C_3N_4 monolayer. Black, orange, and red balls represent C, N, and Li atoms, respectively[58]

Chapter 3: Investigation of the dispersibility of 2D nanomaterials and the key role of Hansen solubility parameters

3.1 Hansen solubility parameters

Until 1967, the most applicable way to explore the miscibility of solvents was the determination of the Hildebrand solubility parameters (HP). Since then, Dr. Charles Hansen suggested a new approach of estimation, including three parameters; a) the dispersive (van der Waals) which correspond to the energy from dispersion forces between molecules, labeling as δ_D, b) the polarity, which correspond to the energy from dipolar intermolecular force between molecules, labeling as δ_P and c) hydrogen-bonding aspects of a solvent, a polymer or a pigment, which correspond to the energy of hydrogen bonds between molecules, labeling as δ_H.[59] Few years later, these parameters were named as Hansen Solubility Parameters (HSP) by A. Beerbower, a Hansen's colleague.[60]

Hansen's theory is based on the idea of "like dissolves like" and thus solvents with similar HSP are more likely to form more stable and uniform mixtures than those with remarkably different parameters, overcoming the limitations of HP.[59] More specifically, the HP are suitable in case of nonpolar or slightly polar systems as the theory was based on the hydrocarbon solvents behavior excluding the cases of hydrogen bonding and polar solvents.[59]

It is obvious that Hansen's study was a step beyond the Hildebrand's theory, which allows its application in a wider range of solvents. In that way, molecules' interactions in terms of solubility, dispersibility, swelling and other can be easily explained.[59]

Hansen Solubility Parameters, are divided into the three components, and can be calculated by the equation: $\delta_\tau^2 = \delta_P^2 + \delta_H^2 + \delta_D^2$ (1)

where the typical units are expressed in MPa$^{1/2}$.[59]

The HSP distance, regularly called R_a, is the distance between two molecules and it is a measure of how alike they are. This value, is essentially the net difference between the HSP of two molecules

As lower the R_a between two molecules is, more alike they are. The calculation formula is:

$$R_a = \sqrt{4(\delta_{D1} - \delta_{D2})^2 + (\delta_{P1} - \delta_{P2})^2 + (\delta_{H1} - \delta_{H2})^2} \ (2) \ [59]$$

The factor 4 came up through the experimental evidence as extracted by the spherical HSP plots and proposed by Hansen and colleagues.[59]

3.2 Three-dimensional Hansen's Space - The HSP sphere

The Hansen's solubility sphere or Hansen's space is a three-dimensional space determined by the provided HSPs of the material of interest. The sphere provides information about how "good" or "bad" is a solvent for a molecule, in fact predicting if a solvent may solubilize a molecule or not, respectively. Therefore, into the sphere all possible "good" solvents are included, while on the outside are designated the "bad" ones. The center of the sphere is considered as the HSP of the molecule of interest. The radius (R_0) defines the boundary that a solvent is considered as "good". Any solvent outside the radius is considered as "bad".[59]

For virtual representation, a Hansen sphere can be plotted according to the conditions described above. A Relative Energy Difference (RED) can be defined in order to assist the observer to distinguish if a solute is within the dispersibility space or not.

The RED value is given by the equation: $\text{RED} = \dfrac{R_a}{R_0}$ (3)[59]

When RED < 1, then $R_a < R_0$, meaning that the molecule of interest is soluble in the solvent or in the case of two solvents molecules' that they are miscible; in simple words, they are alike. Alternatively, when RED > 1, then $R_a > R_0$, implying that the molecules of interest are not alike.

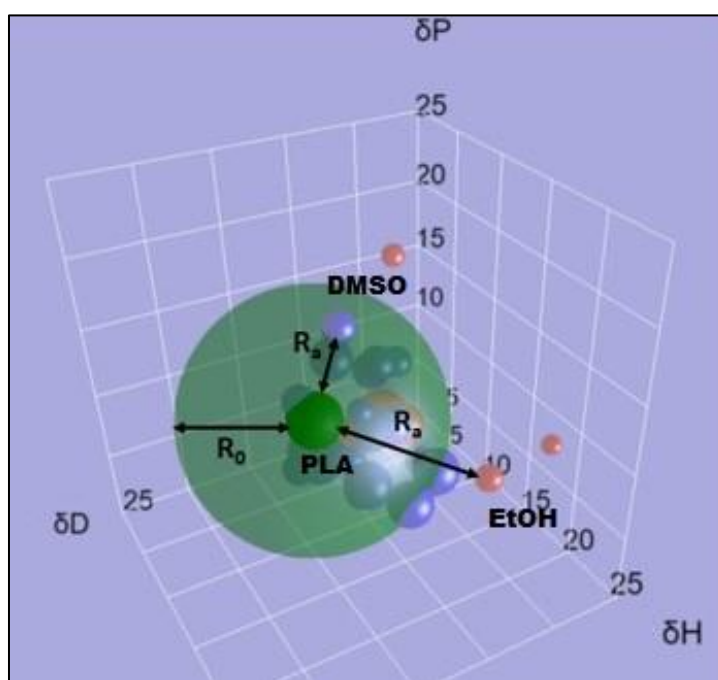**Figure 20**: The HSP sphere of PLA.[61]

Hansen provided an example and presented the HSP sphere of polylactic acid (PLA), as depicted in **Figure 20**, with HSPs $\delta_D = 18.72$, $\delta_P = 7.00$, and $\delta_H = 7.00$, respectively.[61] The small bold green sphere stands for the HSP of the PLA, where R_a is the distance of the PLA's HSP from the HSP of each solvent while R_0 is the radius of the boundary sphere. The blue small spheres represent the good solvents for the molecule of PLA and are located within the sphere or at the boundaries where $R_a < R_0$. The small red spheres represent the bad solvents that are located outside the sphere at a larger distance than the radius R_0, where $R_a > R_0$.[61] For example, dimethyl sulfoxide (DMSO) (HSPs: 18.4, 6.4, 10.2, respectively) is considered as a good solvent for PLA while ethanol (HSPs: 15.8, 8.8, 19.4) is considered as bad (**see Figure 20**).

Finally, it should be noted that a simple way to designate good and bad solvents for a molecule of interest is labeling with the values 1 and 0, respectively. Therefore, in case of PLA a good solvent gets a score of 1, while a bad one is denoted by 0.[61]

Chapter 4: Experimental Section

Preparation of carbon nitride dispersions

The bulk form of carbon nitride was used in this thesis, synthesized by the polymerization of melamine under high temperature,[62] as depicted in **Figure 21** below. More specifically, melamine was put into a sealed crucible and heated at 600 °C for 2 hours into a muffle furnace with a ramp rate of about 3 °C/min for both the heating and cooling processes. The obtained g-C$_3$N$_4$ was yielded as a yellow powder. Bulk g-C$_3$N$_4$ was provided by Transparent and Conductive Materials group.

Figure 21: Synthesis of g-C$_3$N$_4$[57]

The bulk material was dispersed in a range of 19 different solvents, to cover a broad range of physical characteristics, in terms of polarity, surface tension, boiling point etc, using an initial concentration of 1 mg/mL. This was achieved utilizing an ultrasonication probe setup. The solvents used are listed in Table 1.

Table 1: The solvents used in this study to disperse g-C$_3$N$_4$ and their abbreviations.

	Solvent name	Abbreviation
1	Deionized water	DH$_2$O
2	methanol	MeOH
3	ethanol	EtOH
4	isopropyl alcohol	IPA

5	1-butanol	BuOH
6	acetone	Act
7	ethylene glycol	EG
8	acetic acid	AcOH
9	o-xylene	Xyl
10	ethyl acetate	EA
11	hexane	Hex
12	toluene	Tol
13	acetonitrile	MeCN
14	dimethylformamide	DMF
15	dimethyl sulfoxide	DMSO
16	tetrahydrofuran	THF
17	N-methyl pyrrolidone	NMP
18	chloroform	CF
19	tetrachloroethylene	TCE

Each sample was prepared according to the following procedure:

10 mg of $g\text{-}C_3N_4$ were placed into a vial (22 mL) and then it was filled with 10 mL of the solvent of interest. Each sample was then sonicated for 30 min (twice) at 50 kHz using a probe assisted method, with a five-minute interval break between the two sonication circles. During the sonication process the vial was sunk into an ice bath to avoid overheating. Finally, each sample was centrifuged at 2500 rpm, with Relative Centrifugal Force (RCF) at 1006 g, for 20 min and the supernatant was collected. Next, 2 mL of the supernatant of each dispersion were carefully removed and placed into a vial (2 mL). Then the vial was placed on a hotplate to evaporate the solvent. It should be noted that each vial was weighed before and after the evaporation of the solvent. Therefore, the mass of the

remaining carbon nitride in each of the 19 vials could be determined and thus the experimental HSPs could be determined.

Except from the experimental determination of the concentration of each dispersion, as described above, the concentration was also calculated through the Beer - Lambert's law. Towards this, the absorption coefficient of the dispersions was required. In this context a calibration line was plotted for each dispersion separately and its slope corresponds to the absorption coefficient.

To plot the calibration line, a diagram of the absorption versus concentration was formed. In our case, the mean absorption coefficient was determined according to the following procedure:

Four very low concentrations of g-C_3N_4 dispersions (2.5-10 μg/mL) were formed by selecting four of the nineteen solvents in which g-C_3N_4 exhibited higher dispersibility. The absorption of each dispersion at a high wavelength (500 nm) was measured via UV-vis spectroscopy. Thereafter, the obtained absorption values of each dispersion were divided by the cell path of the cuvette used, and a unique point was resulted. Finally, a line was plotted based on the resulted twenty points. Its slope corresponds to the average extinction coefficient, which may result in the average absorption coefficient value, according to the equation: $a = \frac{4\pi k}{\lambda}$, where α is the absorption coefficient, k is the extinction coefficient and λ is the selected wavelength where the absorption is stronger (in the specific case it was at 500 nm). The resulted average absorption coefficient of g-C_3N_4 will be further used to extract any conclusions about the dispersibility of g-C_3N_4 in each solvent.[63] Therefore, through Beer Lambert's law the concentration of g-C_3N_4 was in each solvent determined and compared with the respective values extracted experimentally, as above mentioned.[64]

The Beer Lambert's equation is $A = a \cdot C \cdot d$, where A is the absorbance, a is the absorption coefficient and d is the length of the light path.

Chapter 5: Characterization – Results and Discussion

5.1 XRD pattern of g-C₃N₄
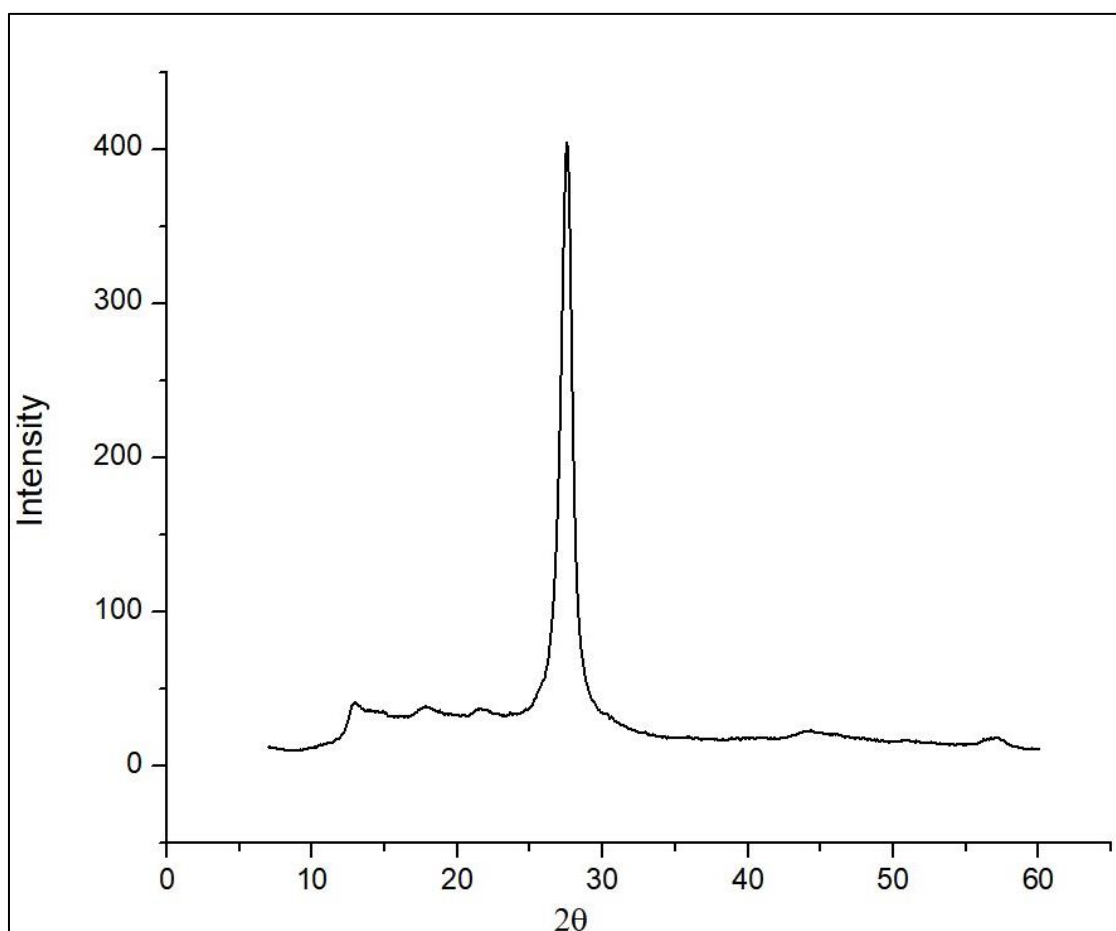
Figure 22: The XRD pattern of g-C$_3$N$_4$.

X-ray diffraction is a powerful nondestructive technique for characterizing crystalline materials. It provides information on structures, phases, preferred crystal orientations (texture), and other structural parameters, such as average grain size, crystallinity, strain, and crystal defects.[65] g-C$_3$N$_4$ was also characterized by X-Ray Diffraction (XRD), using a RINT-2000 Rigaku Diffractometer and its pattern is displayed in **Figure 22**. The XRD data were collected over a 2θ range of 5°- 60° with a step of 0.01° at a wavelength of λ=1.5406 Å. In addition, the average number of sheets was determined by the Scherrer relation.

The pattern presents a characteristic strong peak at 2θ = 27.5° and a small one at 2θ = 13.0°. The main peak at 27.5 ° is attributed to the (002) plane corresponding to a d-spacing of 0.336 nm. This often refers to the interlayer distance of bulk g-C$_3$N$_4$. Lower angles indicate a larger d-spacing between the layers. Moreover, the

peak at $2\theta = 13.0°$ corresponds to the 100 plane with a d-spacing of 0.680 nm and represents the flat structural motive of the repeating tri-s-triazine units (intra-layer d-spacing).[66,67]

The d-spacing was extracted using the Bragg's law: $d = \dfrac{n \cdot \lambda}{sin\theta}$, where $\lambda = 1.5406$Å representing the wavelength of the incident X-rays, n = 1 representing the diffraction order, and 2θ corresponds to the angle of diffraction.

To calculate the number of layers of bulk g-C_3N_4, the crystallite size (D) was calculated through the Scherrer's formula:

$$D = \dfrac{K \cdot \lambda}{\beta \cdot cos\theta},$$ where K = 0.9 Scherrer's constant, $\lambda = 1.5406$ Å, the wavelength of the incident X-Ray beam, β is the full width at half maximum (FWHM) in rad and θ is the peak position (angle).

Then the average number of layers was calculated by the division of the average crystallite size with the interlayer distance (d-spacing = 0.336 nm). From the above equation the crystallite size was calculated to be 18.65 nm and as a result the average number of g-C_3N_4 layers was determined to be ~56.

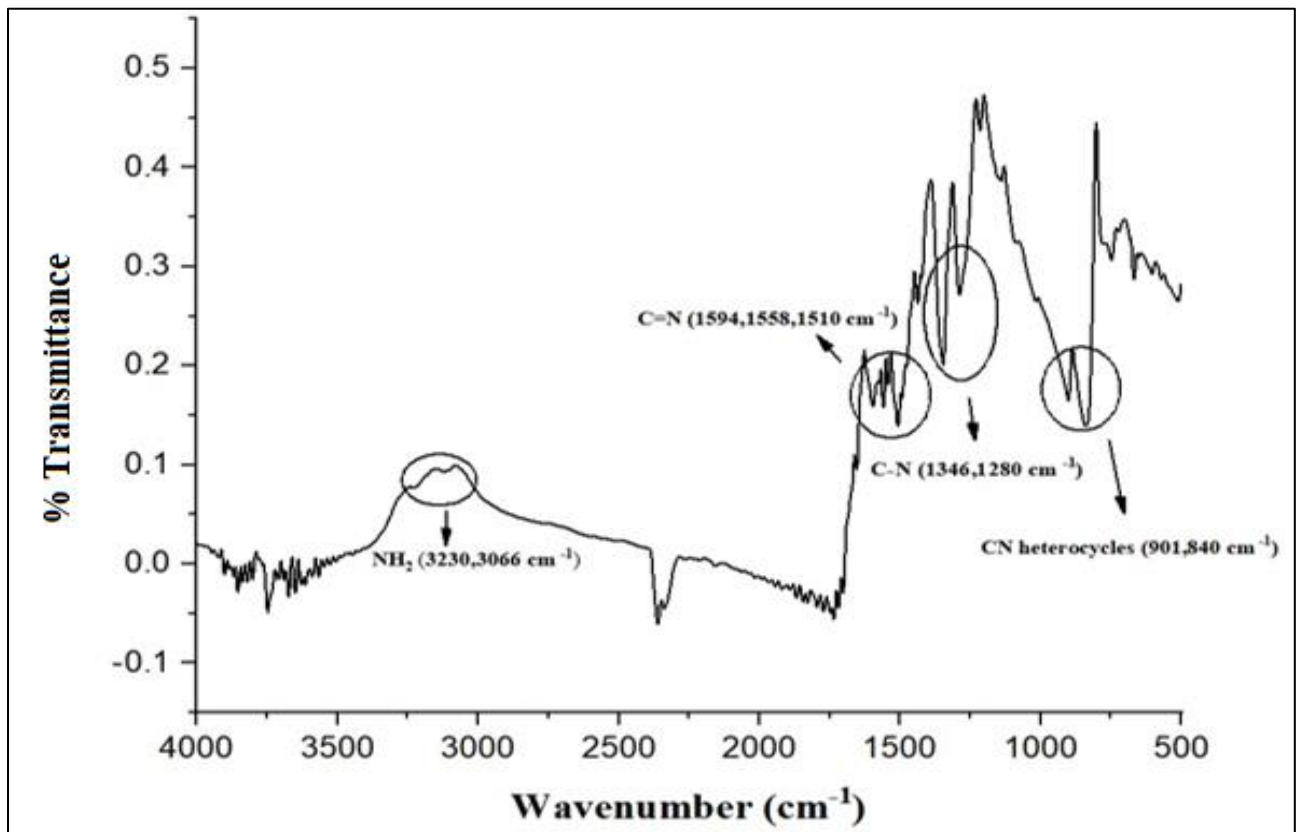## 5.2 ATR-IR and Raman spectroscopy characterization

**Figure 23**: The ATR-IR spectrum of bulk g-C_3N_4.

ATR-IR is a non-destructive spectroscopic technique that provides information related to the presence or absence of specific functional groups, as well as the chemical structure of polymer materials.[68]

Figure 23 shows the Attenuated Total Reflectance spectrum of g-C$_3$N$_4$ (ATR). The transmittance bands near 3230 and 3066 cm^{-1} are attributed to the stretching modes of -NH$_2$ and =NH groups, respectively and imply the presence of remained amino groups. The bands between 1510-1594 cm^{-1} correspond to C=N stretching and similarly the bands at 1280 and 1346 cm^{-1} are attributed to C-N stretching. Finally, the peaks at 840 and 901 cm^{-1} correspond to the triazine model due to condensed CN heterocycles.[69]

All of the above results are in accordance with the literature, confirming the g-C$_3$N$_4$ network which consists of tri-s-triazine units, cross-linked with N atoms in a trigonal formation, as depicted in **Figure 24**.**Error! Bookmark not defined.**
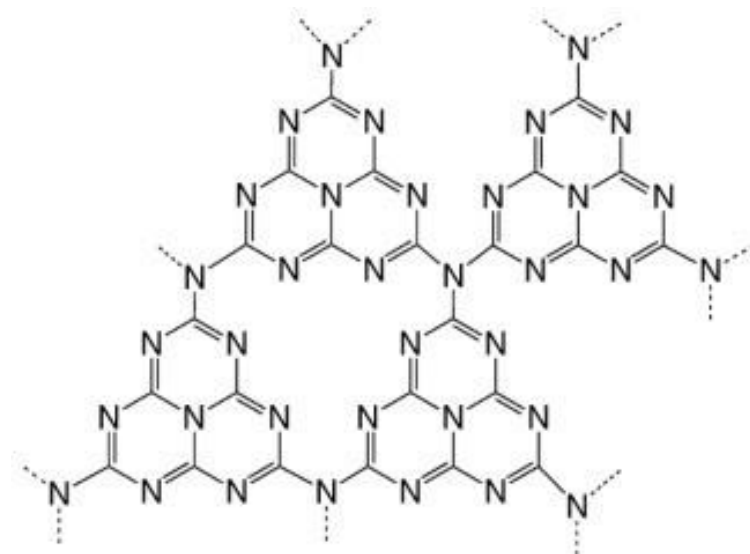
Figure 24: g-C$_3$N$_4$ network **Error! Bookmark not defined.**
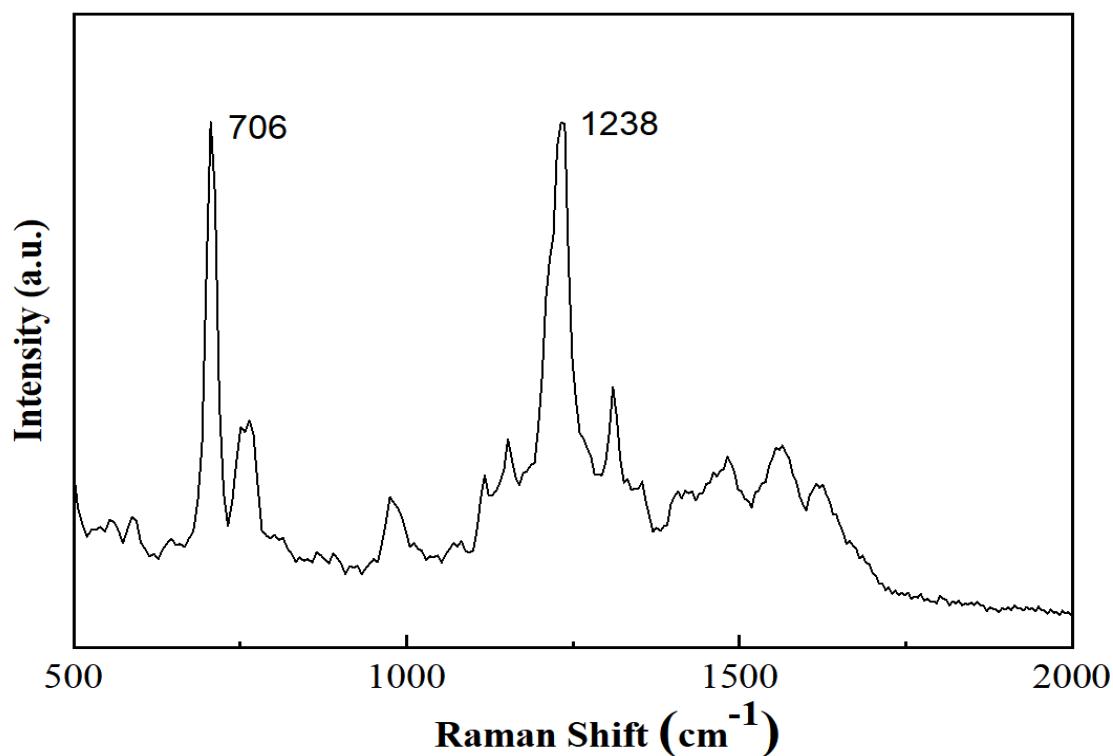
Figure 25: Raman spectrum of g-C3N4

Raman spectroscopy is a powerful, non-invasive tool that offers information on disorder, edge and texture boundaries, thickness, doping etc. of graphene and 2D graphene-like materials like g-C_3N_4.[70]

As excitation source, a 1064 nm light was used, and **Figure 25** shows the Raman spectrum of bulk g-C_3N_4. The peak at 706 cm^{-1} corresponds to the breathing mode of sp^2 atoms in heptazine rings known as D peak, disorder band or defect band. The peak around 1238 cm^{-1} is attributed to the stretching vibration mode of C-N heterocycles known as G band. Usually, a band near 1560 cm^{-1} appears if the g-C_3N_4 powder consists of many impurities. In the current case, this band is not visible which proves the high purity of the synthesized material.[71]

5.3 Optical observation

As can be observed even by the naked eye, the dispersions of g-C_3N_4 depicted in **Figure 22** after the centrifugation, cannot be well-dispersed or the dispersibility is relatively low in MeCN, EA, IPA, Hex, Tol, Xyl, DH$_2$O and Act. Therefore, their supernatants are almost clear. On the other hand, in THF, NMP, TCE and AcOH, g-C_3N_4 seems to be slightly dispersed, as a light blur can be observed. Finally, g-C_3N_4 exhibits higher dispersibility in MeOH, EtOH, DMF, DMSO, EG, BuOH, as a concentrated white color can be seen.

A comparison, between the stability of the dispersions immediately after their preparation and after two weeks took place and is shown in Figure 22 as well. It is evident that g-C$_3$N$_4$ remained dispersed in EtOH, DMF, DMSO and EG where the dispersions were very stable, and a slight precipitation occurred. In the case of MeOH and BuOH, although the initial samples were well dispersed, mild precipitation occurred. Nevertheless, the two samples can be still considered as adequately stable dispersions. On the contrary, the dispersions in THF, NMP and TCE were not stable at all and almost precipitated right after their preparation, demonstrating a very poor dispersibility in these solvents.

Despite the low initial concentration of the dispersion in AcOH, after two weeks the concentration remained almost the same, presenting a slightly better stability than the other "poor" solvents.

As a general observation, all g-C$_3$N$_4$ dispersions were completely or partially settled down with the presence of sediment. In the case of "good" solvents the amount of sediment was significantly lower than in the "poor" ones.

After the two weeks, vials were placed in hotplate for solvents evaporation for the HSPs calculation through weighing the remaining mass of g-C$_3$N$_4$.
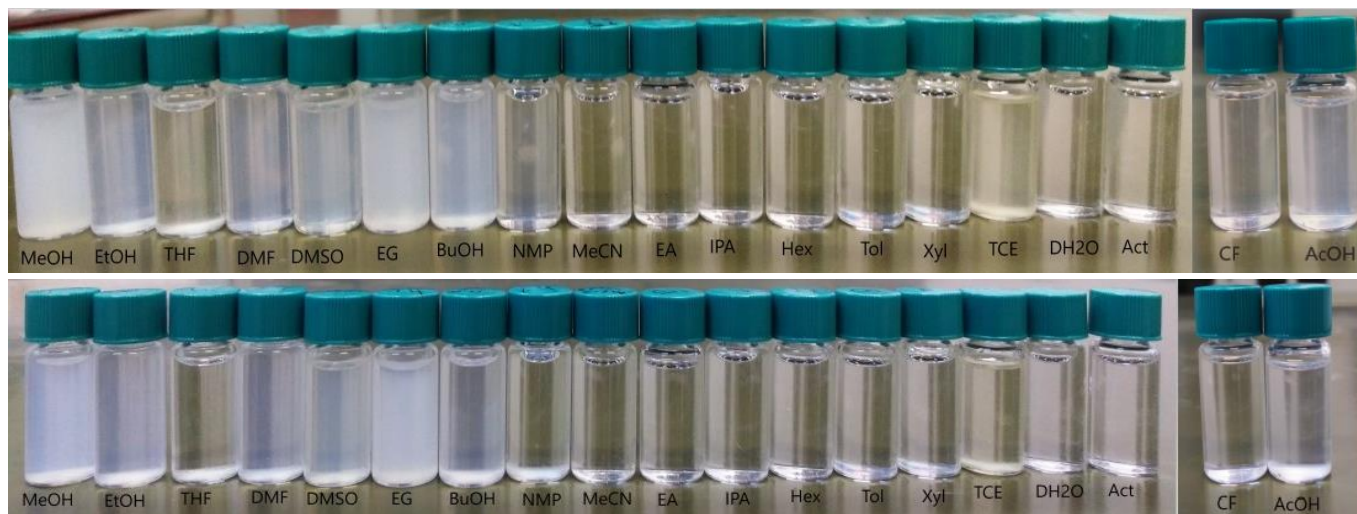
Figure 26: Photo of the samples of g-C$_3$N$_4$ immediately after probe-assisted sonication, centrifugation and supernatant isolation (top) and after 2 weeks (bottom).

After weighing, the remaining mass in every solvent, the concentration of g-C$_3$N$_4$ could be calculated. All concentrations are displayed below in mg/mL.

Table 2: Concentration of g-C$_3$N$_4$ after solvent's evaporation, as weighted by a Kern 4-digit analytical balance.

| DH$_2$O	MeOH	EtOH	IPA	ButOH	Act	EG	AcOH	Xyl	EA
0.05	0.30	0.20	0.05	0.15	0.05	0.80	0.20	0.30	0.10
Hex	**Tol**	**MeCN**	**DMF**	**DMSO**	**THF**	**NMP**	**CF**	**TCE**	
0.05	0.05	0.10	0.10	0.30	0.30	0.10	0.25	0.20	

5.4 Absorption measurements via UV-vis spectroscopy

The concentration of g-C$_3$N$_4$ in all tested solvents will also be calculated through the Beer-Lambert's law for the HSPs calculation in comparison with the HSPs calculation through weighing the remaining mass. The maximum absorption of each dispersion with unknown concentration was performed through UV-vis spectroscopy, right after the centrifugation. Indicatively, the obtained spectra are shown below, where the absorption is displayed in arbitrary units (a.u.).

The spectra of the good solvents according to **Figure 22** are shown below:
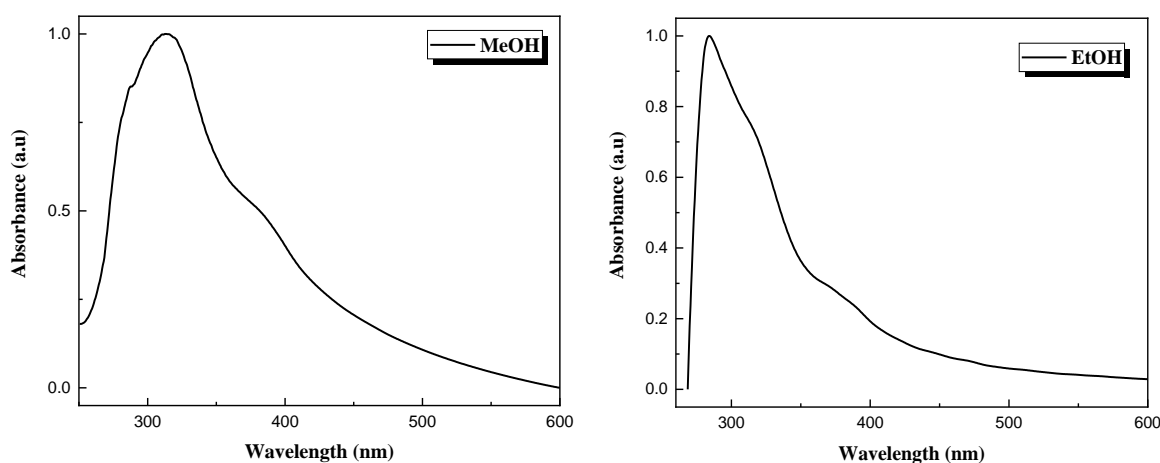
Figure 27: UV-vis absorption spectra of g-C$_3$N$_4$ in MeOH and EtOH
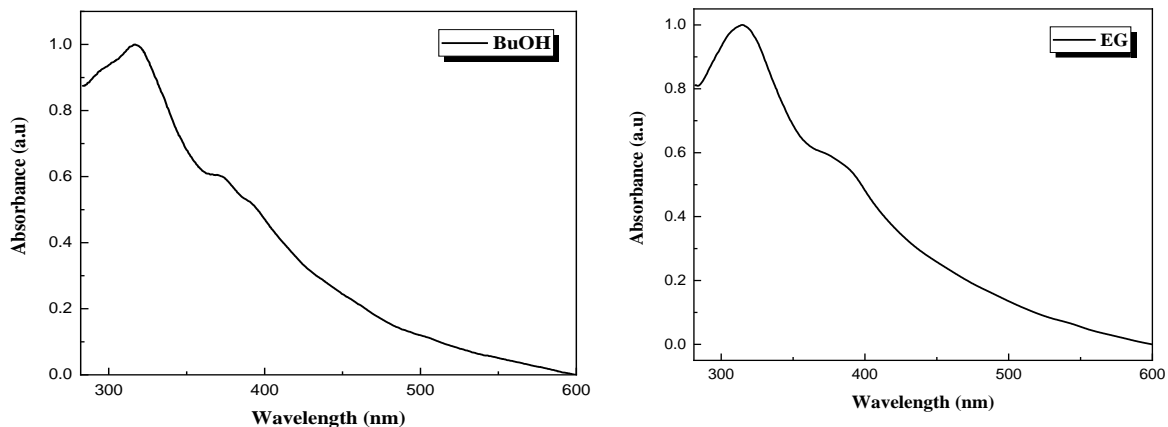
Figure 28: UV-vis absorption spectra of g-C$_3$N$_4$ in BuOH and EG

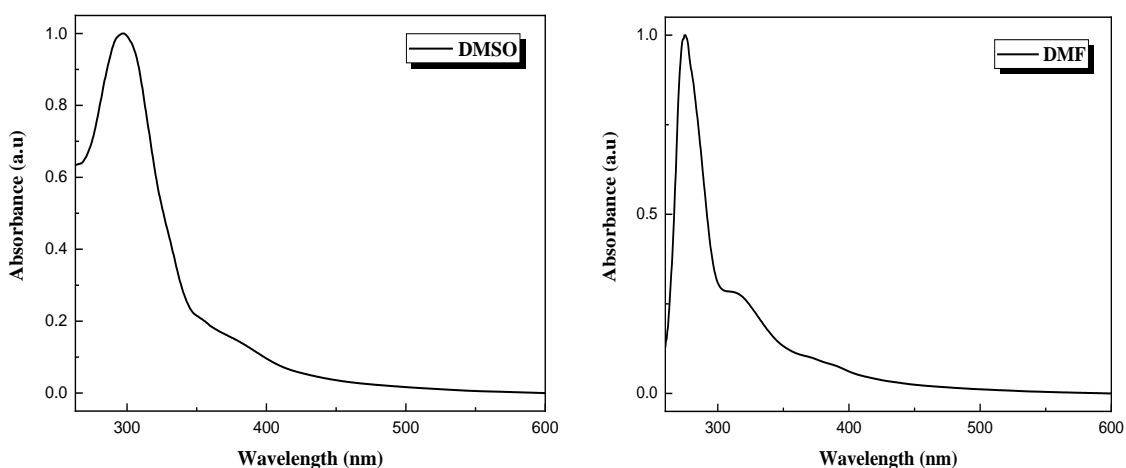**Figure 29**: UV-vis absorption spectra of g-C$_3$N$_4$ in DMSO and DMF

The spectra of the bad solvents according to **Figure 26** are shown below:

Figure 30: UV-vis absorption spectra of g-C$_3$N$_4$ in DH$_2$O and IPA
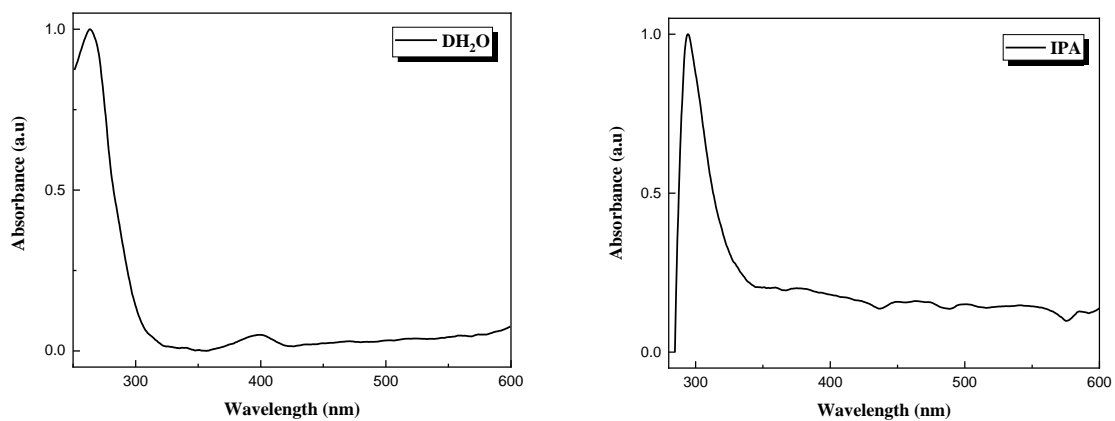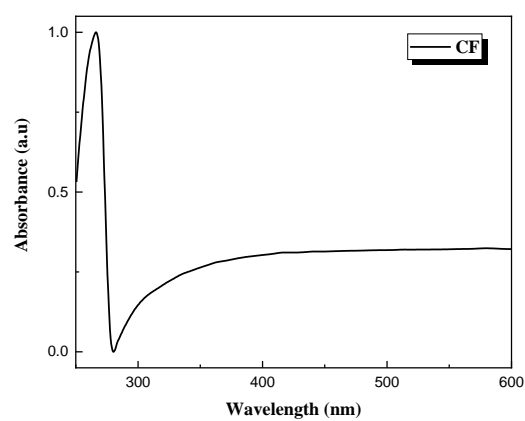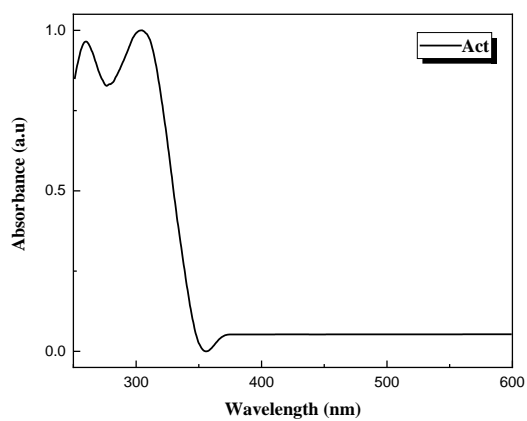
Figure 31: UV-vis absorption spectra of g-C$_3$N$_4$ in Act and CF
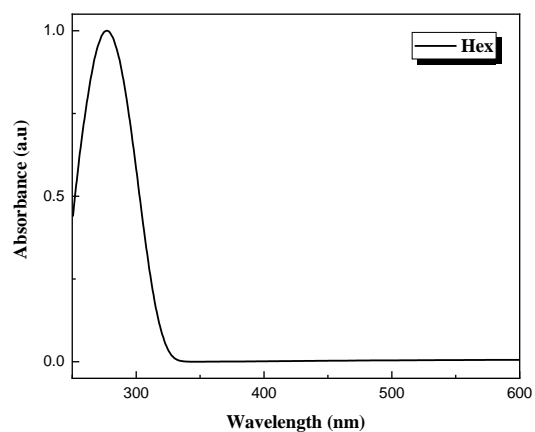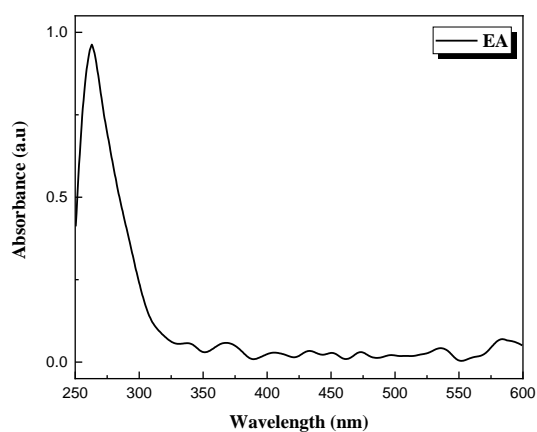
Figure 32: UV-vis absorption spectra of g-C$_3$N$_4$ in EA and Hex
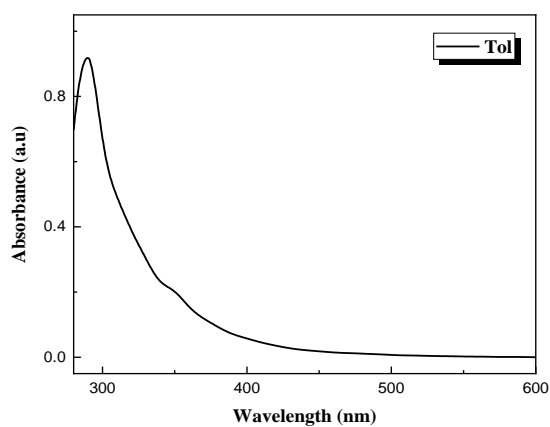
Figure 33: UV-vis absorption spectra of g-C$_3$N$_4$ in Tol and Xyl
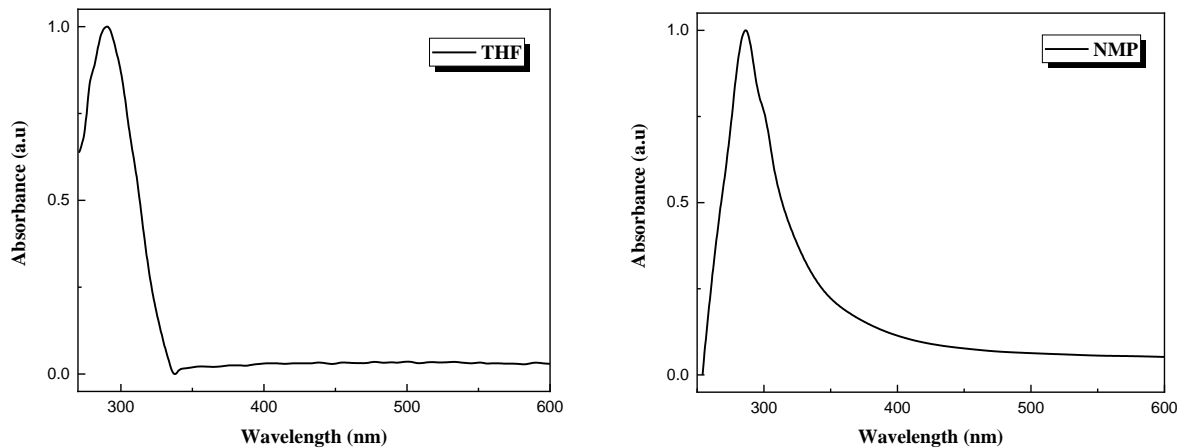
Figure 34: UV-vis absorption spectra of g-C$_3$N$_4$ in THF and NMP

Figure 35: UV-vis absorption spectra of g-C$_3$N$_4$ in AcOH and MeCN

Figure 36: UV-vis absorption spectra of g-C$_3$N$_4$ in TCE

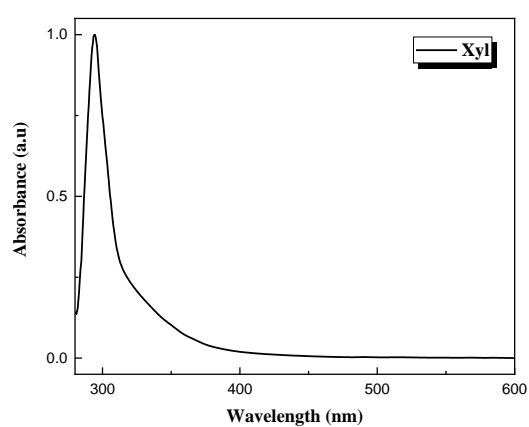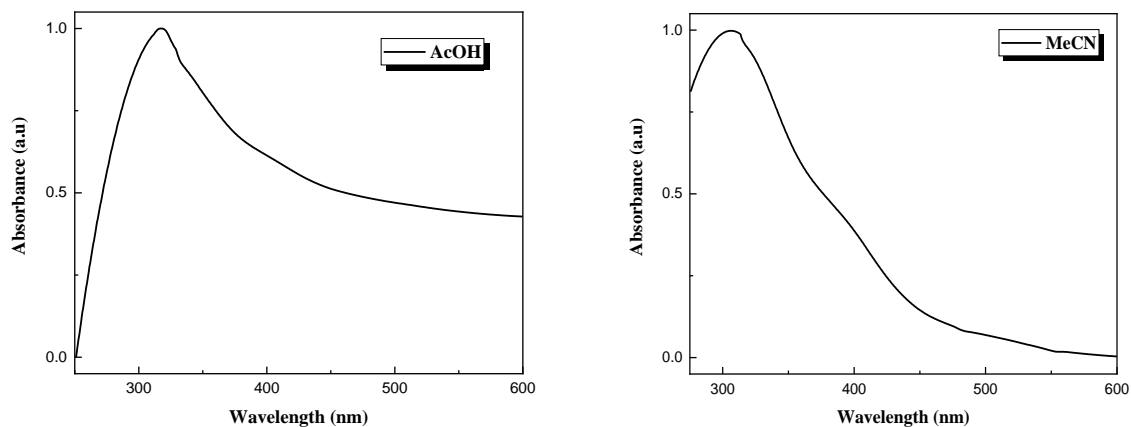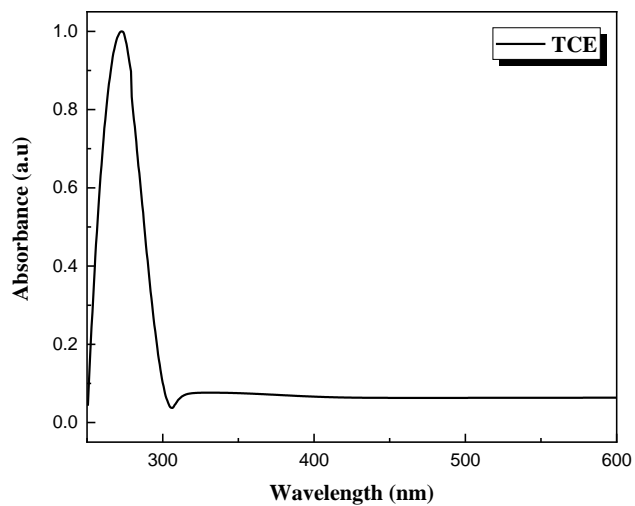The above UV-vis spectra were measured after baseline and background correction at 25 °C. Any difference in shape between the provided spectra can be assigned to bandgap shifting after exfoliation where the indirect bandgap of bulk material shifts to direct bandgap of nanosheets due to the quantum confinement effect.[72]

5.5 Calculation of HSP of carbon nitride

All HSP values used in this thesis for common solvents are listed in **Table 2**. These were extracted by the Three-Dimensional Solubility Parameter and Solvent Diffusion Coefficient by Charles Hansen.[61] In the same table, the values of g-C_3N_4 are also presented, as taken upon the weighing of the remaining mass of each dispersion, after the complete evaporation of the solvent.

<p align="center">Table 3: The HSP values of the solvents used</p>

HSP/Solvents	$\delta_D(\sqrt{Mpa})$	$\delta_P(\sqrt{Mpa})$	$\delta_H(\sqrt{Mpa})$	C_{C3N4} (mg/ml)
DH$_2$0	15.50	16.00	42.40	0.05
MeOH	15.10	12.30	22.30	0.30
EtOH	15.80	8.80	19.40	0.20
IPA	15.80	6.10	16.40	0.05
ButOH	16.00	5.70	15.80	0.15
Act	15.50	10.40	7.00	0.05
EG	17.00	11.00	26.00	0.80
AcOH	14.50	8.00	13.50	0.20
Xyl	17.60	1.00	3.10	0.30
EA	15.80	5.30	7.20	0.10
Hex	14.90	0.00	0.00	0.05
Tol	14.90	1.40	2.00	0.05
MeCN	15.30	18.00	6.10	0.10
DMF	17.40	13.70	11.30	0.10
DMSO	18.40	16.40	10.20	0.30
THF	16.80	5.70	8.00	0.30
NMP	18.00	12.30	7.20	0.10
CF	17.80	3.10	5.70	0.25
TCE	18.80	5.10	9.40	0.20

The above HSP values of the common solvents (**Table 2**) are needed for the calculation of HSP of carbon nitride using the equation: $<\delta i> = \dfrac{\sum C_{C3N4.} \cdot <\delta_i>}{\sum C_{C3N4.}}$ (4)

As a result, the HSPs values were found to be $<\delta_D> = 16.71 \sqrt{MPa}$, $<\delta_P> = 8.78 \sqrt{MPa}$, $<\delta_H> = 14.44 \sqrt{MPa}$, and $<\delta_\tau> = 23.77 \sqrt{MPa}$ as given from the equation (1).

Comparing with the HSPs in the literature[53]: $<\delta_D> = 17.8 \sqrt{MPa}$, $<\delta_P> = 10.8 \sqrt{MPa}$, $<\delta_H> = 15.4 \sqrt{MPa}$ and $<\delta_\tau> = 25.9 \sqrt{MPa}$, calculated HSPs are pretty close except $<\delta_P>$ where a small deviation can be observed.

5.5.1 Determination of the final concentrations of g-C$_3$N$_4$ dispersions

The final concentrations of g-C$_3$N$_4$ dispersions were calculated through the Beer-Lambert's law. From this equation, the absorption coefficient is missing, and its calculation requires a calibration line to be plotted. The line was the linear fit of the concentrations of 4 low concentration dispersions (2.5 µg/ml, 5 µg/ml, 7.5 µg/ml, 10 µg/ml) versus their absorption measurements divided by the cell length. The slope of the line represents the absorption coefficient of the material. The extinction coefficient will be calculated as it was mentioned above in the experimental section.

The above reported low concentrations of g-C$_3$N$_4$ dispersions were prepared through tip sonication in 5 different solvents, considered as the solvents with the higher concentration of g-C$_3$N$_4$ according to the dispersions presented in **Figure 26**. First, 100 µg of g-C$_3$N$_4$ weighed and sonicated in 10 ml of each of the 5 solvents. The three lower concentrations for each solvent were achieved upon dilution of the dispersion with the highest concentration. The respective absorbance in each concentration was performed by UV-vis spectroscopy. The absorbance measurements of the 4 low concentrations were made at a wavelength of 500 nm as the dispersions are required to be transparent according to the literature.[53] The calibration line is shown below in **Figure 37**.
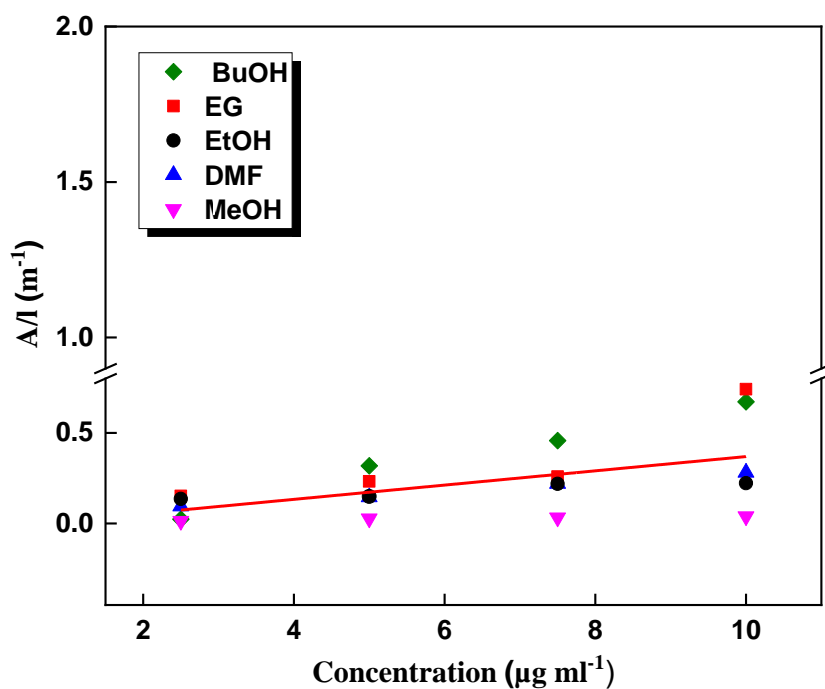
Figure 37: The calibration line of g-C$_3$N$_4$. The slope of the line represents the absorption coefficient of the material.

The slope of the line is 39.36 L/g·m which corresponds to the absorption coefficient of g-C$_3$N$_4$. Finally, the concentration of the dispersions can be calculated through the Beer Lambert's law and are shown in **Table 3**. Similar calibration lines were extracted for each solvent; so, an average calibration line could be extracted as representative for all solvents. In this way, an average absorption coefficient was extracted for g-C$_3$N$_4$. In **Figure 37**, BuOH presents the highest absorbance and MeOH the lowest one, in arbitrary units.

Table 4: The concentration values of the dispersions of carbon nitride, as calculated through the Lambert-Beer law and as weighed through a-4 digit analytical balance

Solvent	C_3N_4 Concentration (μg/ml)	C_{C3N4} (mg/ml) (4-digit balance)
DH_2O	8.97	0.05
MetOH	722.3	0.30
EtOH	116.3	0.20
IPA	62.4	0.05
BuOH	183.3	0.15
Act	145.02	0.05
EG	764.7	0.80
AcOH	142.4	0.20
Xyl	39.89	0.30
EA	2.51	0.10
Hex	0.102	0.05
Tol	20.47	0.05
MeCN	39.89	0.10
DMF	177.85	0.10
DMSO	553.35	0.30
THF	33.97	0.30
NMP	52.46	0.10
CF	21.35	0.25
TCE	238.6	0.20

In order to calculate the above concentrations, we selected the wavelength at 500 nm where solutions need to be transparent according to Beer-Lambert's law.

5.5.2 Estimation of the calculated HSPs for carbon nitride

After calculating the concentration of the dispersions, the HSPs of carbon nitride could be calculated, as the concentration of the dispersions and the HSPs of the solvents were the key factors towards the calculation of the HSPs of g-C$_3$N$_4$. Similar to the theoretical calculations of the HSPs of carbon nitride, δ_D, δ_P and δ_H were calculated through the equation (4) and finally δ_τ through the equation (1).

HSPs for carbon nitride were found to be: $<\delta_D> = 16.58$ $\sqrt{MPa}$, $<\delta_P> = 11.12$ $\sqrt{MPa}$, $<\delta_H> = 17.01$ $\sqrt{MPa}$ and $<\delta_\tau> = 26.23$ $\sqrt{MPa}$.

The determination of the Hansen Solubility Parameters of carbon nitride resulted in the calculation of the R$_a$ distance as previously mentioned (equation 2). The R$_a$ values are shown in Table 5.

Table 5: The R$_a$ values of the dispersions

Solvent	R$_a$
DH$_2$O	25.94
MetOH	6.59
EtOH	3.67
IPA	5.29
BuOH	5.67
Act	10.27
EG	9.03
AcOH	6.27
Xyl	17.33
EA	11.52
Hex	20.60
Tol	18.20
MeCN	13.15
DMF	6.50
DMSO	9.35

THF	10.52
NMP	10.29
CF	28.17
TCE	25.71

As mentioned above (**Chapter 3**), R_a represents the distance between g-C_3N_4 and the solvent's Hansen Parameters in the Hansen space. The lower the R_a is, the more alike are the molecules. When the R_a value is smaller or equal to the R_0 (Hansen sphere radius), thus the RED can be calculated, and solvents can be categorized as good or bad. In this work, the R_0 value for carbon nitride was difficult to be calculated. However, the R_a values were calculated through the equation (2) and correlated to the concentration values. A comparison between the values presented in Table 4 and the concentration values of the dispersions (**Table 3**) was done to investigate if a pattern is formed, whether the concentration of the dispersions depends on the R_a. In general, no distinguished trend was observed for the relationship between R_a and dispersibility.
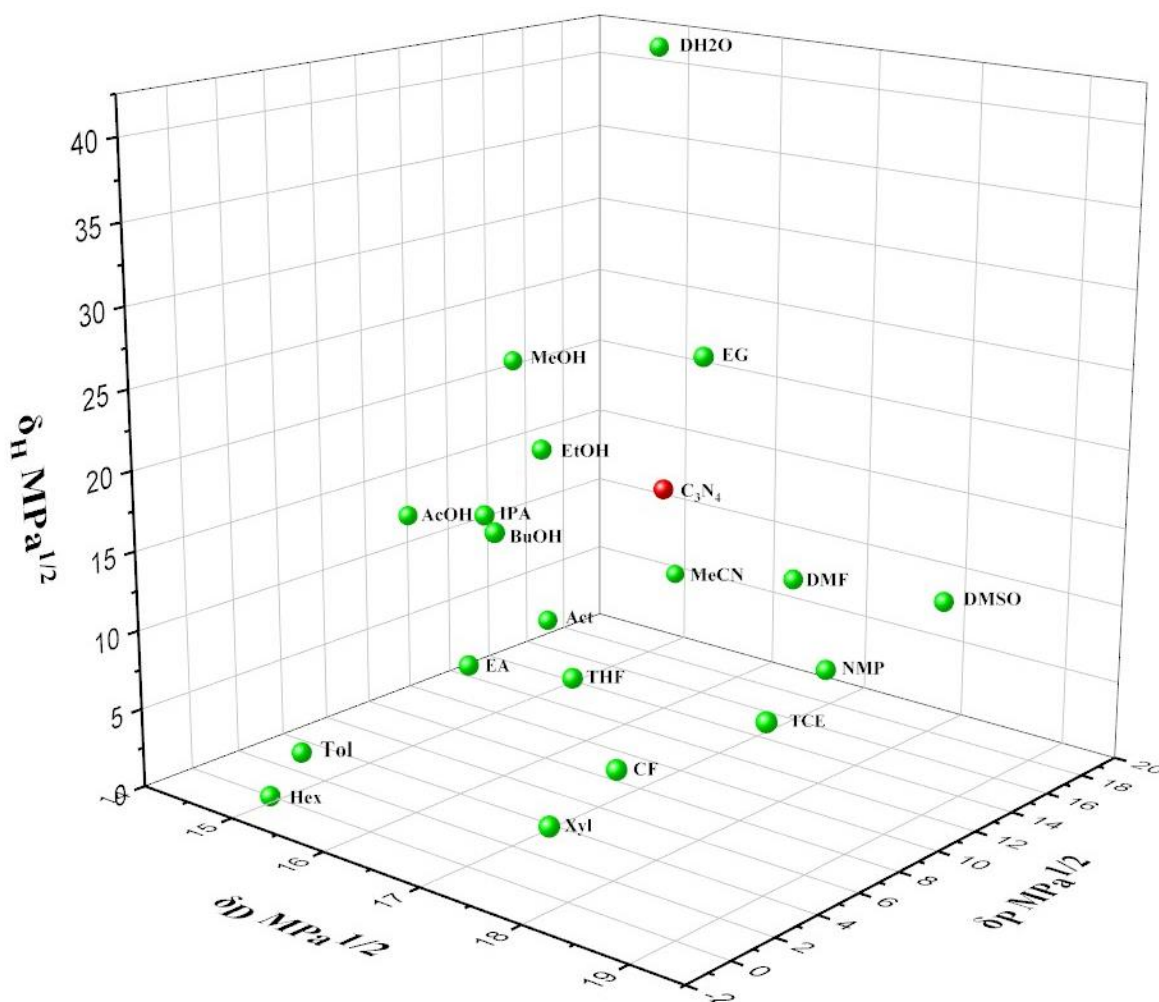
Figure 38: Coordinates (HSP) of carbon nitride and the 19 solvents in a Hansen 3D space

The 3D Hansen space provides information about how miscible two molecules are, according to the R_a and R_0 values. With the absence of R_0, **Figure 38** can be explained as the 3D space, where the green spheres represent the HSP of the solvents and the red one the HSPs of carbon nitride. As closer to the green spheres the red one is, it is more likely they are miscible (i.e., to form homogeneous dispersion). Most of the above green spheres which are closer to the red one, tend to be the solvents where g-C_3N_4 exhibited excellent dispersibility. However, the speculation that the closer a green sphere is, g-C_3N_4 exhibits better dispersibility in this solvent (MeCN, IPA, EtOH, Act, THF) could not be adopted as an absolute norm. On the other hand, the green spheres which are away the red sphere represent the solvents where g-C_3N_4 displays very low dispersibility including DH_2O, Hex, Tol, Xyl and so on.

All of the above values are listed in **Table 6**:

Table 6: The boiling point, HSP, the calculated concentration and the R_a values of all solvents.

Solvent	BP (^{O}C)	δ_D (MPa$^{1/2}$)	δ_P (MPa$^{1/2}$)	δ_H (MPa$^{1/2}$)	δ_τ (MPa$^{1/2}$)	C (μg/ml)	R_a
DH$_2$O	100	15.5	16	42.4	47.89	8.97	25.94
MetOH	56	14.7	12.3	22.3	29.41	722.3	6.59
EtOH	78	15.8	8.8	19.4	26.52	116.3	3.67
IPA	82	15.8	6.1	16.4	23.58	62.4	5.29
BuOH	118	16.0	5.7	15.8	23.20	183.3	5.67
Act	132	15.5	10.4	7.0	19.94	145.02	10.27
EG	56	17.0	11.0	26.0	32.95	764.7	9.03
AcOH	118	14.5	8.0	13.5	21.37	142.4	6.27
Xyl	204	17.6	1.0	3.1	17.90	39.10	17.33
EA	202	15.8	5.3	7.2	18.15	2.51	11.52
Hex	61	14.9	0.0	0.0	14.90	0.102	20.60
Tol	263	14.9	1.4	2.0	15.10	20.47	18.20
MeCN	82	15.3	18.0	6.1	24.40	39.89	13.15
DMF	197	17.4	13.7	11.3	24.86	177.85	6.50
DMSO	76	18.4	16.4	10.2	26.68	553.35	9.35
THF	77	16.8	5.7	8.0	19.46	33.97	10.52
NMP	34	18.0	12.3	7.2	22.96	52.46	10.29
CF	68	17.8	3.1	5.7	18.95	21.35	28.17
TCE	87	18.8	5.1	9.4	21.63	238.6	25.71

6. Conclusions

The present thesis intended to investigate the dispersion behavior of graphitic – Carbon Nitride (g-C_3N_4) in an extended range of solvents, and to calculate its Hansen Solubility Parameters. In addition, the bulk material was thoroughly characterized in powder form, by spectroscopic techniques like UV-Vis, ATR-IR and XRD. The Hansen's theory was implemented in order to interpret the affinity of carbon nitride with certain solvents or lack thereof. The calculated HSPs were

$<\delta_D> = 16.58\ \sqrt{MPa}$, $<\delta_P> = 11.12\ \sqrt{MPa}$, $<\delta_H> = 17.01\ \sqrt{MPa}$ and $<\delta_\tau>=26.23$

$\sqrt{MPa}$, which are very close to the previously reported in the literature ($<\delta_D> =$

$17.8\ \sqrt{MPa}$, $<\delta_P> = 10.8\ \sqrt{MPa}$, $<\delta_H> = 15.4\ \sqrt{MPa}$ and $<\delta_\tau>=25.9\ \sqrt{MPa}$)[53] and

with the theoretically determined HSPs $<\delta_D> = 16.71\ \sqrt{MPa}$, , $<\delta_P> = 8.78\ \sqrt{MPa}$

,$<\delta_H> = 14.44\ \sqrt{MPa}$ and $<\delta_\tau>= 23.77\ \sqrt{MPa}$. It is obvious that the calculated in the present thesis HSPs values are more accurate than those in the literature as the ultrasonic probe provides a higher exfoliation degree and therefore higher dispersibility.

Although the Hansen theory has been proven to be a reliable tool towards the investigation of dispersibility, it should be noted that the experimental determination of HSPs, as in the case of this thesis, is semi-empirical and demands devotion since it is a very sensitive approach, as previously described. The classification of a solvent as good or bad depends considerably on the subjectivity of the observer, implying that the calculated HSPs of g-C_3N_4 may differ from the actual values.

On top of that, dispersions as colloidal systems tend to agglomerate affecting the calculation of HSPs, while the synthetic parameters of g-C_3N_4 may affect the hydrogen bonding parameter (δ_H) value. This fact is attributed to the percentage of the remaining amine groups on the g-C_3N_4 sheet of the final product which can vary depending on the preparation conditions.[53]

Hansen's theory suggests that a molecule that can be dissolved in a solvent, usually tends to have similar HSPs. In this thesis, this fact was verified in the cases of MeOH, EtOH, BuOH, DMSO and DMF in which high dispersibility was observed and thus the concentration of g-C_3N_4 was respectively high. Although, Hansen's theory is usually correct in some cases the results may not be in complete agreement with theory. High dispersibility and concentration were also observed in the case of EG although the HSP is not so close. Conversely, solvents

with much lower or higher HSPs than the g-C$_3$N$_4$ ones, showed poor dispersibility and lower concentration. Such solvents were DH$_2$O, Act, EA, THF, Hex, MeCN, Tol, CF and Xyl.

Finally, two solvents with a small HSPs deviation from these of g-C$_3$N$_4$, presented a different behavior than the expected ones. AcOH showed low concentration and thus poor dispersibility although its HSPs are very close with the HSPs of g-C$_3$N$_4$. In contrast, TCE presented higher concentration and dispersibility compared with other solvents with similar HSPs.

IPA and NMP although their HSPs with g-C$_3$N$_4$ HSPs are close, they showed poor dispersibility and low concentration which are not in accordance with the Hansen's theory.

To sum up, according to the literature, it was expected that solvents with high values of hydrogen bonding related Hansen parameter (δ_H = 10-25 Mpa$^{1/2}$) can be considered as appropriate solvents for the exfoliation and dispersion of g-C$_3$N$_4$. This conclusion can be extracted due to the fact that strong hydrogen-bonding interactions occur between the g-C$_3$N$_4$ layers that come up with the presence of remaining amine groups located on its non-ideal structure.[53] This notion is in accordance with the behavior of g-C$_3$N$_4$ in the most solvents as presented in this work. However, no norm was observed to correlate the solvents' physicochemical characteristics with the dispersibility of carbon nitride.

References

[1] Majdoub et al. Acs nano 2020, 14, 12390–12469

[2] Parveen et al., J. Mater. Chem. A 2016, 4, 233–240

[3] Quan et al. Sci Rep. 2014, 4, 5639

[4] Agnoli et al. J. Mater. Chem. A, 2016,4, 5002-5025

[5] Li et al. Chemical Communications, 2016, 52, 10988–10991

[6] Sahoo et al. J. Mater Res Bull. 2014, 10, 049

[7] Wang et al. Applied Surface Science, 2013, 273, 302–309

[8] Chu et al. Materials Science and Engineering: C, 2017, 81, 452-458

[9] Niu et al. New J. Chem., 2014, 38, 2269-2272

[10] Quilez-Bemejo et al. Carbon., 2020, 165 434-454

[11] Gong et al. Science, 2009, 323, 760–764

[12] Qu et al. ACS Nano, 2010, 4, 1321-1326

[13] Liu et al. Chem. Int. Ed. ,2011, 50, 3257-3261

[14] Guo et al. N. Carbon Mater. ,2016, 30, 352-362

[15] Bandosz et al. Carbon Materials for Catalysis New York, 2008, 45-92

[16] Puziy et al. Carbon ,2020, 157, 796-846

[17] McKee et al. Carbon, 1984, 22, 507-511

[18] Allardice et al. Carbon, 1970, 8, 375-385.

[19] Jang et al. J. Mater. Chem. A., 2018, 6, 7351-7356.

[20] Bo et al.Phys. Chem. Chem. Phys., 2013, 15, 2459-2465.

[21] Yang et al. Chem. Int. Ed., 2011 ,50, 7132-7135.

[22] K. Preuss Chempluschem ,2019, 84, 457-464.

[23] Minsik et al. J Mater Chem., 2007, 17, 1656-1659

[24] Shih et al. Physica E*: Low-Dimensional Systems and Nanostructures, 2020, 118, [113894]

[25] Qiang et al. NanoRes., 2020, 13, 18–37

[26] Agrawal et al. J. Chem. Phys., 2020, 153, 054701

[27] Pal Singh, J. et al., 2020, in Sonochemical Reactions IntechOpen

[28] https://www.britannica.com/technology/calcination

[29] Niu et al.Adv. Funct. Mater. 2012, 22, 4763–4770.

[30] Li, Y et al. Advanced Energy Materials,2016, 6, 1601273

[31] Amiri et. al FlatChem 2018, 8, 40–71

[32] Wang et al., ChemSusChem, 2010, 3, 435–439

[33] Montigaud et al. Journal of Materials Science, 2000, 35, 2547–2552.

[34] Seung Jae et al. Carbon, 2009, 47, 1585-1591

[35] Zhihong Zhang et al. Journal of the American Chemical Society, 2001 123 , 7788-7796

[36] Gu et al. Carbon, 2003, 41, 2674-2676

[37] Jilin et al. RSC Advances, 2016, 6, 23272–23278

[38] https://www.corrosionpedia.com/definition/5493/electrochemical-deposition

[39] R M Florea et al. IOP Conf. Ser.: Mater. Sci. Eng., 2019, 591, 012014

[40] Lotsch et al. Chemistry of Materials, 2006, 18, 1891–1900

[41] Mortazavi et al. Computational Materials Science, 2015, 99, 285–289.

[42] Konofaos et al. Journal of applied physics. ,2002, 91, 9915

[43] Derradji et al. Thin solid Films ,2005, 482, 258–263.

[44] Giusto et al M. Adv. Mater. 2020, 32, 1908140.

[45] Changchao et al. ACS Appl. Mater. Interfaces 2020, 12, 53571–53591

[46] Arazoe et al. Nat. Mater. 2016, 15, 1084-1089

[47] Jia et al. Front. Mater. 2019, 6, 52.

[48] Zhuang et al. ACS Applied Materials & Interfaces, 2019, 11, 12770-12776

[49] Nicholas et al. Critical Reviews in Solid State and Materials Sciences, 2020, 46, 189-217

[50] Ni et al. Renew. Sust. Energy. Rev. 2007, 11, 401–425

[51] He et al. J. Catal., 2017, 354, 231–235

[52] Ragupathi et al. Optik, 2019, 202, 163601.

[53] Ayán-Varela et al. ACS Applied Materials & Interfaces, 2015, 7, 24032–24045

[54] Li et al RSC Advances, 2015, 5, 24507–24512.

[55] Niu et al. Advanced Functional Materials, 2012, 22, 4763–4770.

[56] Shen et al. Nanotechnology, 2018, 29, 412001.

[57] Rono et al. Critical Reviews in Solid State and Materials Sciences 2021 ,46, 189-217

[58] Hussain et al. J. Phys. Chem. C, 2016, 120, 25180–25188

[59] Hansen Solubility Parameters | Hansen Solubility Parameters (hansen-solubility.com)

[60] C. M. Hansen, Hansen Solubility Parameters, A User's Handbook, (2000).

[61] The HSP Sphere | Hansen Solubility Parameters (hansen-solubility.com)

[62] Wang et al. Nanoscale, 2015, 7, 5152–5156

[63] Hernandez, et al. Nature Nanotech, 2008, 3, 563–568

[64] https://www.edinst.com/blog/the-beer-lambert-law/

[65] Rajiv Kohli, Developments in Surface Contamination and Cleaning, 2019, 12, 23-105
[66] Lotsch et al. Chemistry of Materials, 2006, 18, 1891–1900.

[67] Alizadeh et al. RSC Advances, 2019, 9, 13096-13103.

[68] Peter Larkin, Chapter 3 - Instrumentation and Sampling Methods, 2011,27-54
[69] Minsik, Journal of Materials Chemistry - J. Mater. Chem., 2007,17, 1656-1659

[70] Childres et al. New Developments in Photon and Materials Research., 2013, 403-418.

[71] Wang et al, Photon. Res., 2018, 6, 307-313

[72] Hui et al. Journal of Alloys and Compounds ,2017, 690, 669-676